Available online at www.sciencedirect.com
ScienceDirect
Geochimica et Cosmochimica Acta 73 (2009) 1359–1381
Geochimica et Cosmochimica Acta
www.elsevier.com/locate/gca

Arsenite sequestration at the surface of nano-$Fe(OH)_2$, ferrous-carbonate hydroxide, and green-rust after bioreduction of arsenic-sorbed lepidocrocite by *Shewanella putrefaciens*

Georges Ona-Nguema [a,b], Guillaume Morin [a,*], Yuheng Wang [a], Nicolas Menguy [a], Farid Juillot [a], Luca Olivi [c], Giuliana Aquilanti [d], Mustapha Abdelmoula [e], Christian Ruby [e], John R. Bargar [f], François Guyot [a], Georges Calas [a], Gordon E. Brown Jr. [b,f]

[a] *Institut de Minéralogie et de Physique des Milieux Condensés (IMPMC), Université Paris 6, Université Paris 7, IPGP, CNRS, 140, rue de Lourmel, 75015 Paris, France*
[b] *Department of Geological and Environmental Sciences, Surface & Aqueous Geochemistry Group, Stanford University, Stanford, CA 94305-2115, USA*
[c] *XAFS Beamline, ELETTRA, AREA Science Park, 34012 Basovizza, Trieste, Italy*
[d] *BM29 European Synchrotron Radiation Facility (ESRF) BP220, 38043 Grenoble Cedex, France*
[e] *Laboratoire de Chimie Physique et Microbiologie pour l'Environnement (LCPME), UMR 7564 CNRS, Université Nancy 1, 405, rue de Vandœuvre, 54600 Villers-lès-Nancy, France*
[f] *Stanford Synchrotron Radiation Laboratory, SLAC, MS 69, 2575 Sand Hill Road, Menlo Park, CA 94025, USA*

Received 18 January 2008; accepted in revised form 3 December 2008; available online 24 December 2008

Abstract

X-ray Absorption Fine Structure (XAFS) spectroscopy was used in combination with high resolution transmission electron microscopy (HRTEM), electron energy loss spectroscopy (EELS), X-ray energy dispersive spectroscopy (XEDS), X-ray powder diffraction, and Mössbauer spectroscopy to obtain detailed information on arsenic and iron speciation in the products of anaerobic reduction of pure and As(V)- or As(III)-adsorbed lepidocrocite (γ-FeOOH) by *Shewanella putrefaciens* ATCC 12099. We found that this strain of *S. putrefaciens* is capable of using Fe(III) in lepidocrocite and As(V) in solution or adsorbed on lepidocrocite surfaces as electron acceptors. Bioreduction of lepidocrocite in the absence of arsenic resulted in the formation of hydroxycarbonate green rust 1 [$Fe^{II}_4Fe^{III}_2(OH)_{12}CO_3$: GR1($CO_3$)], which completely converted into ferrous-carbonate hydroxide ($Fe^{II}_2(OH)_2CO_3$: FCH) over nine months. This study thus provides the first evidence of bacterial reduction of stoichiometric GR1(CO_3) into FCH. Bioreduction of As(III)-adsorbed lepidocrocite also led to the formation of GR1(CO_3) prior to formation of FCH, but the presence of As(III) slows down this transformation, leading to the co-occurrence of both phases after 22-month of aging. At the end of this experiment, As(III) was found to be adsorbed on the surfaces of GR1(CO_3) and FCH. After five months, bioreduction of As(V)-bearing lepidocrocite led directly to the formation of FCH in association with nanometer-sized particles of a minor As-rich $Fe(OH)_2$ phase, with no evidence for green rust formation. In this five-month experiment, As(V) was fully converted to As(III), which was dominantly sorbed at the surface of the $Fe(OH)_2$ nanoparticles as oligomers binding to the edges of $Fe(OH)_6$ octahedra at the edges of the octahedral layers of $Fe(OH)_2$. These multinuclear As(III) surface complexes are characterized by As–As pairs at a distance of 3.32 ± 0.02 Å and by As–Fe pairs at a distance of 3.50 ± 0.02 Å and represent a new type of As(III) surface complex. Chemical analyses show that the majority of As(III) produced in the experiments with As present is associated with iron-bearing hydroxycarbonate or hydroxide solids,

* Corresponding author. Fax: +33 1 44 27 37 85.
E-mail address: guillaume.morin@impmc.jussieu.fr (G. Morin).

0016-7037/$ - see front matter
doi:10.1016/j.gca.2008.12.005

reinforcing the idea that, at least under some circumstances, bacterial reduction can promote As(III) sequestration instead of mobilizing it into solution.

1. INTRODUCTION

Arsenic is a toxic metalloid involved in important health issues due to its presence as a contaminant in water resources in many parts of the world as a result of anthropogenic activities (Morin and Calas, 2006) or natural processes (Nriagu, 2002; Vaughan, 2006). High arsenic concentrations in some ground waters typically derive from the weathering of As-bearing minerals (Armienta et al., 2001; Smedley and Kinniburgh, 2002), geothermal sources (Wilkie and Hering, 1998), or the release of As adsorbed on mineral surfaces (Nickson et al., 1998; Harvey et al., 2002; Akai et al., 2004; Islam et al., 2004; van Geen et al., 2004; Gault et al., 2005; Charlet and Polya, 2006). Indeed, a major control of the aqueous concentration, mobility, and cycling of arsenic is its sorption to and desorption from mineral surfaces. Fe-(oxyhydr)oxides are among the most important sorbents of arsenic in the environments. Batch uptake experiments coupled with As K-edge X-ray Absorption Fine Structure (XAFS) spectroscopy on reaction products have shown that arsenic forms inner-sphere adsorption complexes on Fe(III)-(oxyhydr)oxides including ferrihydrite (Waychunas et al., 1995; Ona-Nguema et al., 2005; Canies et al., 2005), goethite (Manning et al., 1998; Farquhar et al., 2002; Manning et al., 2002; Ona-Nguema et al., 2005), lepidocrocite (Randall et al., 2001; Manning et al., 2002; Ona-Nguema et al., 2005), hematite (Ona-Nguema et al., 2005), and maghemite (Manning et al., 2002; Morin et al., 2008). Fe(II)–Fe(III)-containing minerals such as green rusts and magnetite, which can form by bacterial reduction of Fe(III)-(oxyhydr)oxides (Lovley et al., 1987; Cooper et al., 2000; Ona-Nguema et al., 2002a, 2004; Zachara et al., 2002; Glasauer et al., 2003; Zegeye et al., 2005), have also been shown to scavenge a fraction of the soluble arsenic species (e.g., Coker et al., 2006; Wang et al, 2008). For example, Dixit and Hering (2003) found significant uptake of As(III) by magnetite at pH 8 and showed that magnetite, ferrihydrite, and goethite have similar affinities for As(III). Similarly, Randall et al. (2001) showed that As(V) can adsorb on hydroxysulphate green rust, and Root et al. (2007) reported the possible association of arsenite with a mixed Fe(II,III) solid, with a local structure similar to that of green rust, in high-iron sediments from North Haiwee Reservoir (Olancha, CA).

In addition to sorption on mineral surfaces, a variety of microorganisms influences arsenic mobility and geochemistry (Newman et al., 1998; Stolz and Oremland, 1999) using different metabolic processes, including oxidation (Wilkie and Hering, 1998; Joanne et al., 2002), reduction (Dowdle et al., 1996; Ahmann et al., 1997), and methylation reactions (Bentley and Chasteen, 2002) that strongly control arsenic speciation in the environment. For example, iron-respiring bacteria (IRB) are capable of strongly affecting arsenic mobility in anoxic environments by reducing Fe(III) in As-bearing Fe-minerals (Nickson et al., 2000; McArthur et al., 2001; Bose and Sharma, 2002; Oremland and Stolz, 2003; Horneman et al., 2004; Islam et al., 2004; van Geen et al., 2004; Harvey et al., 2005). However, reduction of Fe(III) in green rusts by IRBs has not been reported, and the impact of such reductive dissolution on the release of adsorbed contaminants as well as the nature of biogenic Fe(II)-containing reaction products has not been documented.

In experiments with *Shewanella alga*, an IRB that does not respire As(V), Cummings et al. (1999) demonstrated that reduction of Fe(III) in synthetic scorodite ($FeAsO_4 \cdot 2H_2O$) resulted in the release of As(V) and Fe(II) into solution. Using XAFS spectroscopy, this earlier study revealed that the valence states of Fe and As in the solid-phase product were identical to those in solution (i.e., Fe(II) and As(V)) (Cummings et al., 1999). Moreover, van Geen et al. (2004) pointed out that arsenic is mobilized from Bangladesh sediment only after orange Fe(III)-oxyhydroxides have been reduced to gray or black solid phases containing Fe(II) or Fe(II,III), although the location of this reduction process in the soil/sediment column, resulting in As release, has recently been challenged and is thought by some to take place in near-surface sediments rather than at Holocene aquifer depths (Polizzotto et al., 2005, 2008). By comparing incubations and leaching results, the study by van Geen et al. (2004) suggests that arsenic is concentrated in a relatively labile phase as the sediment is progressively reduced. Consequently, microorganisms naturally present in Bangladesh aquifers can mobilize much of this arsenic fraction from sufficiently reduced sediment, perhaps without the need for extensive iron dissolution (van Geen et al., 2004).

Recently, Kocar et al. (2006) examined arsenic elution from columns loaded with ferrihydrite-coated sand presorbed with As(V) at circumneutral pH, using *Shewanella putrefaciens* strain CN-32 and other microorganisms to reduce Fe(III) and/or As(V). Although As(III) was the only arsenic oxidation state detected in the porewater and in As-bearing solid species upon column breakdown, it is not clear if *S. putrefaciens* actually has a dissimilatory arsenate reductase. Anaerobic experiments with *S. putrefaciens* in which As(V) is the sole electron acceptor are required to determine if this bacterium can indeed reduce As(V) to As(III). Despite the importance of arsenic mobilization in reducing groundwaters and abundant evidence that microbial organisms play an important role in mobilizing arsenic, the nature and mineralogical properties of the phase(s) controlling arsenic solubility in reducing systems are still poorly documented.

In this study, we have employed batch cultures of *S. putrefaciens* strain ATCC 12099 to investigate the bacterial reduction of aqueous $HAs(V)O_4^{2-}$ as an electron acceptor under anoxic conditions. Strain ATCC 12099 was also incu-

bated under anoxic conditions with As(V)-adsorbed lepidocrocite, As(III)-adsorbed lepidocrocite, and lepidocrocite without arsenic. The main purposes of this study were to (i) determine if this bacterium is capable of reducing As(V) to As(III) when $HAs(V)O_4^{2-}$ is adsorbed on the surface of lepidocrocite, a common well-crystallized hydromorphic soil mineral, or when it is the sole electron acceptor in aqueous solution, and (ii) characterize the biogenic solid phases obtained after γ-FeOOH and hydroxycarbonate green rust reduction in the presence of arsenic. We used As K-edge X-ray Absorption Near Edge Structure (XANES) spectroscopy to determine arsenic oxidation state in the new biogenic solid-phase obtained after the bacterial reduction process and X-ray diffraction and Mössbauer spectroscopy to identify crystalline phases. The molecular speciation of the associated arsenic in the reaction products was determined by comparison with a series of Fe(II)–As(III)-containing model compounds synthesized under anoxic conditions using a combination of As and Fe K-edge EXAFS spectroscopy and HRTEM-EELS-XEDS. This study provides the first observation of $Fe(OH)_2$ nanoparticles (2–5 nm in diameter) produced by dissimilatory reduction of ferric oxyhydroxides by *S. putrefaciens* in the presence of As(V) under anoxic, iron-rich conditions; it also proposes a new mechanism for arsenic sorption onto these $Fe(II)(OH)_2$ nano-phases, which may be relevant to iron-rich anoxic environments.

2. METHODS

2.1. Preparation of *Shewanella putrefaciens* Inoculum

Shewanella putrefaciens strain CIP 59.28, equivalent to the American Type Culture Collection (ATCC) 12099, was obtained from the Collection Institut Pasteur (France). Frozen cells from a stock (frozen in 20% glycerol at −80 °C) were revived under aerobic conditions on trypticase soy agar (TSA, BioMérieux, 51044). They were transferred twice to remove glycerol, and subsequently the colonies were used to prepare a suspension with a target optical density of 1.0 ($\lambda = 600$ nm) in NaCl 0.9%. Then, 15 mL of this suspension were inoculated in 150 mL of trypticase soy broth (TSB, BioMérieux, 51019) in order to initiate the liquid preculture. Cells were grown, continuously agitated at 1000 rpm and 22 °C, harvested after 19 h of culture by centrifugation (10,000*g* at 20 °C for 10 min), and concentrated in 35 mL of TSB, of which 30 mL were inoculated into a 1000 mL batch reactor containing 800 mL of TSB to initiate growth of the main culture. The reactor was continuously agitated at 1000 rpm. Cells were grown to a stationary growth phase (10 h) and harvested by centrifugation (12,000*g* at 20 °C for 15 min), washed twice with NaCl 0.9% sterilized by autoclave (121 °C, 20 min), and concentrated in 50 mL of sterile NaCl 0.9%. Cell suspensions were used to inoculate batches containing aqueous $HAs(V)O_4^{2-}$, pure lepidocrocite, and As(V)- and As(III)-adsorbed lepidocrocite under anoxic conditions. The cell density of the inoculum was measured by the number of colony-forming units (CFU) which was determined by plate counting. For this procedure, 0.2 mL of the bacterial suspension adequately diluted in sterile NaCl 0.9% solution was incorporated into TSA.

2.2. Arsenic-adsorbed lepidocrocite preparation

An aqueous suspension of lepidocrocite was prepared under a nitrogen atmosphere in a glove box by addition of 0.3 g of γ-FeOOH to 26 mL of Milli-Q water. After dispersing the lepidocrocite suspension by ultrasonification (13 mm probe, 40 s, 26 mL of suspension, 140 W, VCX 600, Vibracell) to reduce particle aggregation ($d_{50} = 1.0$ μm), 10 mL of the 10-fold concentrated basic medium were added. 270 μL of a high concentration sodium arsenate (As(V)) or sodium arsenite (As(III)) solution (1 M) were added to the media to reach a final arsenic concentration of 6.0 mM in each culture. The pH was adjusted to 7.3, and the medium was then autoclaved at 120 °C for 20 min. A pH 7.4 aqueous solution containing 1.5 mM of anthraquinone-2,6-disulfonate (AQDS) and 1.125 M of methanoate was prepared in O_2-free Milli-Q water and sterilized by filtration through a 0.2 μm filter. Three mL of this solution were added to the medium. Sample flasks were then kept in the dark at 30 °C for 10 days during arsenate or arsenite uptake on lepidocrocite; only 2.9 mM of As(V) and 2.7 mM of As(III) remained in the respective solutions following uptake. After this incubation period, flasks were inoculated with 6 mL of a cell suspension containing 8.7×10^9 CFU mL^{-1}. The final volume of cultures was 45 mL.

2.3. Colony-forming units counts

The number of colony-forming units (CFU) was determined by plate counting. For this procedure, 0.2 mL of the bacterial suspension adequately diluted in sterile NaCl 0.9% solution was incorporated into TSA.

2.4. Bacterial aqueous arsenate reduction cultures

Experiments in which aqueous $HAs(V)O_4^{2-}$ was reduced by *S. putrefaciens* strain ATCC 12099 were performed under anoxic conditions in batch cultures in the presence of an excess of sodium methanoate (10–15 mM) and sodium arsenate (8.2–9.6 mM). 100 μM of AQDS were added in order to enhance the reduction process. The *S. putrefaciens* cell suspension was added to the medium to obtain $0.1–1.5 \times 10^{10}$ CFU mL^{-1}. The composition of the basic medium is also given in Electronic annex EA-1. The pH, measured after all components had been mixed, was 7.7 ± 0.2. Cultures were incubated at 30 °C in darkness for 4 days in most cases and in a few cases for up to 12 days (not shown). During this incubation period, aliquots were removed at selected time intervals to measure As(V) reduction to As(III). LC-SAX™ SPE cartridges were used to separate inorganic arsenic species (arsenite and arsenate) in a filtered aliquot sample prior to elemental analysis using ICP–AES. Abiotic control experiments (i.e., without cells) were performed under anoxic conditions in the presence of sodium arsenate (8–10 mM), sodium methanoate (10–15 mM), and AQDS (100 μM).

2.5. Bacterial arsenic and lepidocrocite reduction cultures

Experimental studies of the bacterial reduction of pure lepidocrocite and As(V)- and As(III)-lepidocrocite were performed under anoxic conditions in batch cultures with *S. putrefaciens* strain ATCC 12099 (1.2×10^9 CFU mL^{-1}) in the presence of 75 mM of sodium methanoate, 6 mM of sodium arsenate, and 75 mM of lepidocrocite (γ-FeO-OH). 100 μM of AQDS were added to enhance the reduction process. The composition of the basic medium is given in Electronic annex EA-2. The medium was sterilized by autoclave at 120 °C for 20 min., except for the AQDS and methanoate, which were sterilized by filtration through a filter of pore size 0.2 μm. No buffer was used. Solid phases obtained after various incubation periods were harvested by centrifugation (10000*g*, 10 min), washed twice in O_2-free Milli-Q water, and vacuum-dried for 6 days.

For the pure lepidocrocite bioreduction experiment, solids were sampled after two, five, and nine months and are referred to as samples Lp-*Sp* #1, #2, and #3, respectively. For the As(III)-sorbed lepidocrocite bioreduction experiment, solids were sampled after two, five, nine, and twenty-two months and are referred to as samples As(III)Lp-*Sp* #4, #5, #6, and #7, respectively. For the As(V)-sorbed lepidocrocite bioreduction experiment, solids were sampled after two and five months and are referred to as samples As(V)Lp-*Sp* #8 and #9, respectively. All of these solid samples were analyzed by XRD, and only the end-products of the bioreduction experiments (i.e., samples Lp-*Sp* #3, As(III)/Lp-*Sp* #7, and As(V)/Lp-*Sp* #9) were analyzed by Mössbauer and XAFS spectroscopy.

2.6. Model compound preparation

Model compounds consisting of co-precipitation or adsorption of arsenite with or on Fe(II)-hydroxide and green rusts were prepared to help in interpreting HRTEM and XAFS data from the biogenic samples. Two X-ray amorphous Fe(II)–As(III) hydroxide model compounds, referred to as R0.1 and R0.3, were prepared by co-precipitating Fe(II) and As(III) ions at neutral pH with As/Fe (molar ratio) = 0.1 and 0.3, respectively. The synthesis was performed in a JACOMEX® glove box under an N_2 atmosphere (<15 ppm O_2). All reagents used were chemical grade (99.9 wt% purity level), and the solutions were prepared in the glove box with O_2-free milli-Q water. Three mL of a 1 M $FeCl_2 \cdot 4H_2O$ solution and 0.3 mL or 0.9 mL of a 1 M $NaAsO_2$ solution were added to 900 mL O_2-free milli-Q water in 1 L bottles. The pH was then adjusted to 7.0 by adding appropriate quantities of 1 M NaOH solution under agitation. The final volume was increased to 1000 mL with O_2-free milli-Q water. The suspension was agitated for 24 h in the glove box and then filtered through a 0.22 μm membrane. The resulting powder was vacuum-dried and stored in the glove box, and the filtered solution was acidified and also stored in the glove box for further analysis. Polycrystalline $Fe(OH)_2$ (brucite-type structure) was synthesized in the same manner as above, except for the absence of As(III) in the medium.

In addition, As(III) adsorbed-hydroxychloride green rust I, with ideal formula $Fe^{II}_3Fe^{III}(OH)_8Cl$, referred to as As(III)/GR1(Cl), was prepared by adding 1 mL of 0.0668 M $NaAsO_2$ solution to 38 mL of a suspension containing 0.5 g GR1(Cl) with an ionic strength I = 0.1 M. The pH was adjusted to 7.2 and an appropriate volume of NaCl solution was then added to obtain a final volume of 40 mL. GR1(Cl) was previously synthesized by oxidation in air of a ferrous hydroxide suspension in the presence of a slight excess of dissolved ferrous chloride (Refait et al., 1998a,b). A sample of As(III) adsorbed-$Fe(OH)_2$, referred to as As(III)/$Fe(OH)_2$, was prepared in the same manner as the As(III)/GR1(Cl) sorption sample, by using $Fe(OH)_2$ as the substrate.

2.7. Chemical analyses of the solutions

The supernatants from the incubation experiments and from the model compound syntheses were filtered through a 0.22 μm membrane and acidified with HNO_3 in the glove box to avoid precipitation of iron oxides, which would cause a decrease in the concentrations of iron and arsenic in solution. Iron and arsenic concentrations were determined by inductively coupled plasma–atomic emission spectroscopy (ICP–AES) performed on a Jobin-Yvon® JY 238 Ultrace spectrometer, and by graphite furnace atomic absorption spectrometry (GFAAS) on a Unicam® 989 QZ spectrometer, respectively. The Fe and As detection limits for ICP–AES and GFAAS were 0.018 μM and 0.03 μM, respectively.

2.8. X-ray powder diffraction

To avoid oxidation by air, dried samples containing Fe(II) were placed in Lindeman glass tubes of 0.5 mm diameter and sealed with LOCTITE® Super Glue under a nitrogen atmosphere in the glove box ($O_2 \leqslant 15$ ppm). X-ray diffraction (XRD) measurements were performed with Co*Kα* radiation ($\lambda = 0.17889$ nm) on a Panalytical X'Pert Pro MPD diffractometer mounted in the Debye–Scherrer configuration, using an elliptical mirror to obtain a high flux, parallel incident beam and an X'Celerator detector to collect the diffracted beam. Data were recorded in continuous scan mode within the 5–80° 2θ range with a step size of 0.0167°. XRD was carried out twice on each sample, once with and once without NaCl as an internal standard, except for samples Lp-*Sp* #3, As(III)/Lp-*Sp* #7, and As(V)/Lp-*Sp* #9, which were only characterized with the internal standard present.

2.9. Backscattering Mössbauer spectroscopy

Room temperature (RT) backscattering Mössbauer spectroscopy was used to characterize the end-products of the bioreduction experiments, i.e., samples Lp-*Sp* #3, As(III)/Lp-*Sp* #7, and As(V)/Lp-*Sp* #9. Mössbauer spectra were obtained using the miniaturized Mössbauer spectrometer MIMOS II, which was designed and fabricated at the University of Mainz in Germany (Klingelhofer et al., 2004) and was originally developed for exploration of the

planet Mars. The Mössbauer instrument operates in back-scattering measurement geometry and consists of gamma ray and X-ray detectors, a ^{57}Co Mössbauer source (50 mCi), which is embedded in a rhodium metal matrix attached to a titanium holder, the Mössbauer drive and its control unit, and the data acquisition system. The instrument is equipped with four Si-PIN-diode detectors to detect resonantly scattered X-rays (6.4 keV) and γ-rays (14.4 keV) from the surface targets. Samples were prepared in an anaerobic chamber (Coy Laboratory Products), and aliquots (10 mL) were taken from the well-homogenized mineral suspension; iron particles were concentrated by filtration (0.45 μm pore size) and enclosed in an anaerobic cell in plexiglas. Measurements were done by placing the detector head against the Mylar window of a cell in plexiglas which contains the sample under anaerobic conditions. The spectra were fitted with the software Recoil™ (Lagarec and Rancourt, 1997) using Lorentzian or pseudo-Voigt line shapes.

2.10. High resolution transmission electron microscopy (HRTEM), X-ray energy dispersive spectroscopy (XEDS), electron energy loss spectroscopy (EELS)

For TEM analysis, the samples were directly prepared from the anoxic serum flasks sealed with butyl rubber stoppers. About one μL of suspension was extracted from each serum flask and deposited onto a carbon-coated holey grid using syringe and needle. The grids were then immediately transferred into the vacuum chamber of the electron microscope, which was pumped down, causing evaporation of the suspension. Using this protocol, Fe(II) oxidation was found to be negligible, as indicated by EELS spectra of the Fe(II)–As(III) model compounds. HRTEM images and XEDS spectra were taken using a JEOL™ 2100F TEM apparatus. HRTEM data were processed using the ImageJ 1.34r program package, and XED spectra were quantified using the IDFix© v5 program package, taking into account fluorescence yield factors for correcting integral intensities of K emission lines.

2.11. X-ray Absorption Near Edge Structure (XANES) spectroscopy and extended X-ray absorption fine structure (EXAFS) spectroscopy

All XAFS data were recorded on vacuum-dried samples diluted with appropriate amounts of cellulose for either fluorescence or transmission measurements. In order to avoid Fe(II) oxidation by air and to limit As(III) oxidation under the X-ray beam (Ona-Nguema et al., 2005; Morin et al., 2008; Wang et al., 2008), all data were recorded at 10–15 K on all beamlines, using liquid He cryostats. Arsenic K-edge EXAFS data for biogenic samples and of sorption model compounds were recorded in fluorescence detection mode on wiggler beamline 11-2 at the Stanford Synchrotron Radiation Laboratory (SSRL). Arsenic K-edge EXAFS data for co-precipitated model compounds were collected in transmission detection mode on bending magnet beamline 'XAFS' at the ELETTRA synchrotron light laboratory. Fe K-edge EXAFS data for the model compound samples were recorded in transmission detection mode on bending magnet beamline BM29 at the European Synchrotron Radiation Facility (ESRF). Fe K-edge EXAFS data for the biogenic samples were recorded in transmission detection mode on the wiggler beamline 10-2 at SSRL.

XANES and EXAFS data were normalized and extracted using the XAFS program (Winterer, 1997). Least-squares fitting of the unfiltered $k^3\chi(k)$ functions were performed with the plane-wave formalism, using a Levenberg-Marquard minimization algorithm following a previously detailed procedure (Ona-Nguema et al., 2005; Morin et al. 2008; Wang et al. 2008). Theoretical phase-shift and amplitude functions employed in this fitting procedure were calculated with the curved-wave formalism using the *ab-initio* FEFF 8 code (Ankudinov et al., 1998). As–O, As–As, and As–Fe phase-shift and amplitude functions were extracted from the tooeleite ($Fe_6(AsO_3)_4SO_4(OH)_4 \cdot 4H_2O$) crystal structure (Morin et al., 2007). Fe–O, Fe–Fe, and multiple-scattering phase-shift and amplitude functions were extracted from the $Fe(OH)_2$ (brucite-type) structure (Chichagov et al., 1990) using the FEFF 8 code. Further details of the XAFS data acquisition and analysis are given in Supporting Information.

3. RESULTS

3.1. Bacterial arsenate reduction under anoxic conditions

Arsenic reduction experiments were conducted and monitored with *S. putrefaciens* strain ATCC 12099 (Fig. 1a and b) in the presence of sodium arsenate as the sole electron acceptor and sodium methanoate as the electron source under non-growth conditions (i.e., without phosphate addition to the medium). Results show that the As(III) concentration increased with time, (Fig. 1a and b). The specific initial rate of bacterial reduction was 6×10^{-11} μmol h^{-1} CFU^{-1}. These results ndicate that *S. putrefaciens* is able to couple the reduction of As(V) with the oxidation of methanoate under anoxic conditions according to the reaction:

$$HAsO_4^{2-} + HCO_2^- + 2H^+ \leftrightarrow H_3AsO_3 + HCO_3^- \quad (1)$$

The pH increased during reduction of As(V) from 7.8 to a final value of 8.7 ± 0.1 and is probably due to the consumption of protons as shown in reaction (1). The As(V) concentrations measured in the three abiotic (control) assays were 7.9 mM (Fig. 1a) and 9.6 mM (Fig. 1b), showing that no arsenate reduction was observed in these abiotic experiments.

3.2. Color and chemistry changes during (As-adsorbed) lepidocrocite bioreduction

Significant changes occurred in the color of the solid phases formed from the reduction of lepidocrocite by *S. putrefaciens* ATCC 12099 under anoxic conditions. During the biomineralization of pure lepidocrocite, for example, the color of the suspensions changed from orange to green after two months of incubation (sample Lp-*Sp* #1), prior to

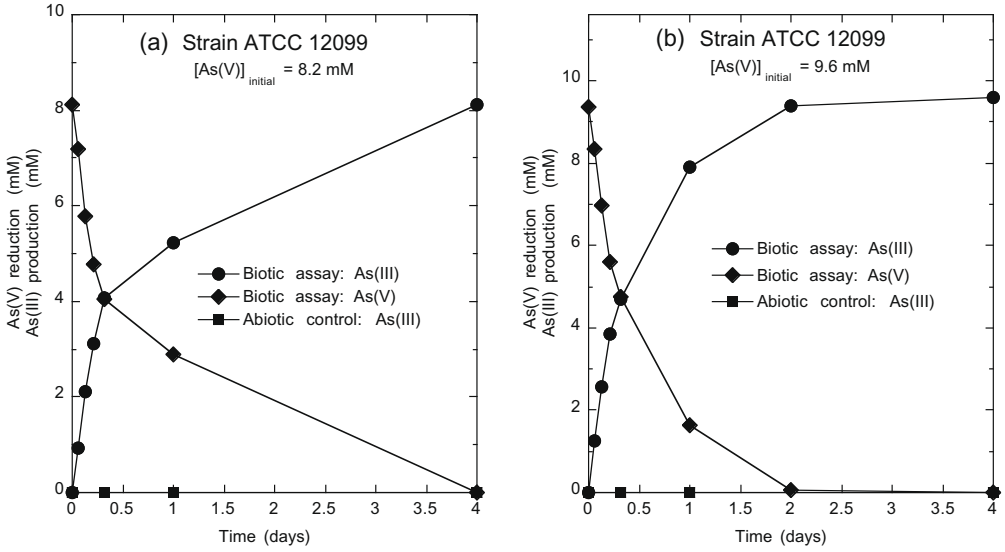

Fig. 1. Reduction of dissolved As(V) by *Shewanella putrefaciens* strain ATCC 12099 with methanoate as the electron donor under anaerobic conditions. (a) Bacterial assay conducted with a cell suspension of 1.0×10^{10} CFU mL^{-1}, 8.2 mM of As(V), and 0.1 mM of anthraquinone-2,6-disulfonate (AQDS) and an excess of methanoate (12 mM). (b) Assay performed with a cell suspension of 1.5×10^{10} CFU mL^{-1}, 9.6 mM of As(V), 0.1 mM of AQDS and an excess of methanoate (15 mM). Symbols in biotic assays: As(V)-aqueous (solid diamonds), and As(III)-aqueous (solid circle). As(III)-aqueous (solid square) measured in abiotic control experiments (i.e., without cells) performed under similar conditions as assays with cells.

becoming blue-green after five months (sample Lp-*Sp* #2), then essentially white to the unaided eye after nine months (sample Lp-*Sp* #3). A similar behavior was observed during the reduction of As(III)-sorbed lepidocrocite, resulting in blue-green suspensions after two, five, and nine months (samples As(III)/Lp-*Sp* #4, #5, and #6, respectively) and a sky-blue suspension after twenty-two months of incubation (sample As(III)/Lp-*Sp* #7). The bioreduction of As(V)-adsorbed lepidocrocite was visually different; the suspensions changed from orange to white after five months of incubation (sample As(V)/Lp-*Sp* #9) with an intermediate dark-orange color after two months (sample As(V)/Lp-*Sp* #8). During these bacterial reduction experiments, pH increased from 7.3 ± 0.1 to 9.1 ± 0.2.

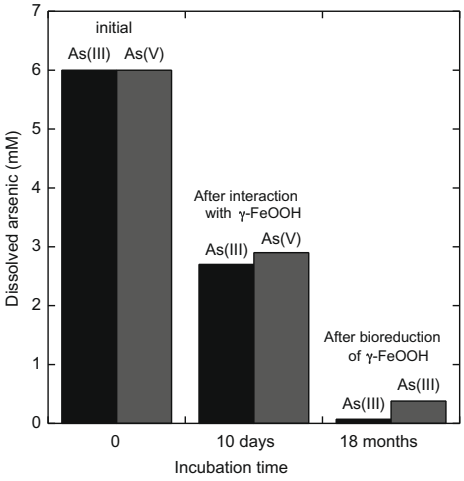

Fig. 2. Concentration of dissolved arsenic before and after bacterial reduction of Fe(III) (and As(V) in arsenic-adsorbed lepidocrocite by *Shewanella putrefaciens* strain ATCC 12099. In black, system in which 6 mM of As(III) were initially mixed with 75 mM of lepidocrocite (γ-FeOOH). In grey, system in which 6 mM of As(V) were initially mixed with 75 mM of lepidocrocite; during this second experiment As(V) is completely reduced into As(III) by *Shewanella putrefaciens* strain ATCC 12099.

Chemical analyses of dissolved arsenic in the supernatants revealed that after 10 days of lepidocrocite interaction with the arsenic-containing solutions (initial arsenic concentrations of 6.0 mM) in the absence of *S. putrefaciens*, only about half of the initial arsenic was associated with the solid phase (Fig. 2, and Table 1). In contrast, after 18 months of aging in the presence of *S. putrefaciens* strain ATCC 12099, the solid phase scavenged 94% of As(V) and 99% of As(III) in the bioreduction experiments of As(V)- and As(III)-adsorbed lepidocrocite, respectively (Fig. 2, and Table 1). Further investigations were then carried out in order to identify the mineral phases responsible for arsenic scavenging after the bioreduction of lepidocrocite and to determine arsenic speciation in these heterogeneous mineral mixtures.

3.3. Mineralogical composition of the (As-)lepidocrocite bioreduction products

The Fe(II)-containing phases formed upon bioreduction of lepidocrocite (with or without As) by *S. putrefaciens* ATCC 12099 were studied by X-ray diffraction (XRD) as a function of incubation time (Fig. 3a–c), and the end-products of these bioreduction experiments were analyzed by room temperature (RT) backscattering Mössbauer spectroscopy and HRTEM–XEDS–EELS.

Table 1
Chemical composition of the dissolved and solid phases in selected samples. Estimated standard deviations (1σ) are given in parentheses and refer to the last digit.

Sample	[A] $[As]_{final}$ (μM)	[B] $[Fe]_{final}$ (μM)	[C] $[As]_{solid}$ (wt%)	[C] $[Fe]_{solid}$ (wt%)
As(III)/Lp 10 days*	2700 (10)	<120	na	na
As(III)/Lp-*Sp* 18 months**	72 (1)	774 (1)	na	na
As(V)/Lp 10 days*	2900 (10)	<120	na	na
As(V)/Lp-*Sp* 18 months**	381 (1)	750 (1)	3.8 (1)	36.0 (1)
As(III)–Fe(II) R0.1	1.3 (1)	155 (1)	4.9 (1)	47.0 (1)
As(III)–Fe(II) R0.3	4.9 (1)	137 (1)	19.6 (1)	46.1 (1)
As(III)/$Fe(OH)_2$	34.7 (10)	804 (1)	0.8 (1)	61.9 (1)
As(III)/GRCl	6.1 (1)	410 (1)	0.9 (1)	54.8 (1)

na, not analyzed.
* After 10 days equilibration of 6000 μM As(III) or As(V) with Lp only.
** After 18 months inoculation with *Shewanella putrefaciens* strain ATCC 12099.
(A) GF-AAS analysis.
(B) ICP-AES analysis.
(C) AAS analysis after dissolution of the solid in HCl 2 M.

3.3.1. Bioreduction of pure lepidocrocite (γ-FeOOH)

The XRD pattern of sample Lp-*Sp* #1 (Fig. 3a) exhibits diffraction maxima characteristic of green rust 1 and of lepidocrocite. The prominent peaks of the former phase with *d*-spacings at $d_{003} = 0.755$ nm, $d_{006} = 0.378$ nm, $d_{012} = 0.267$ nm, $d_{015} = 0.235$ nm, and $d_{018} = 0.197$ nm correspond to those of hydroxycarbonate green rust 1, GR1(CO_3), as previously shown by Ona-Nguema et al. (2002a, 2004) during the bioreduction of γ-FeOOH. The XRD pattern of sample Lp-*Sp* #2 (Fig. 3a) shows diffraction maxima characteristic of GR1(CO_3) and some minor ones ascribed to ferrous-carbonate hydroxide [$Fe^{II}_2(OH)_2CO_3$: FCH], without evidence of lepidocrocite. FCH and NaCl (an internal standard) are the only phases contributing to the XRD pattern of sample Lp-*Sp* #3 (Fig. 3a), indicating complete reduction of Fe(III) in GR1(CO_3). The backscattering Mössbauer spectrum of the end-product sample Lp-*Sp* #3 (Fig. 4) exhibits a single paramagnetic quadrupole doublet D_1 with hyperfine parameters (isomer shift $\delta = 1.14$ mm s^{-1} and quadrupole splitting $\Delta E_Q = 2.03$ mm s^{-1}) characteristic of Fe(II) in octahedral sites and ascribable to the FCH phase (Fig. 4), confirming the complete reduction of Fe(III) in GR1(CO_3). Our Mössbauer hyperfine parameters are close to those obtained at RT in transmission mode by Kukkadapu et al. (2005). These results show, for the first time, that iron-respiring bacteria are capable of utilizing Fe(III) in GR1(CO_3) as the electron acceptor to form FCH.

3.3.2. Bioreduction of As(III)-adsorbed lepidocrocite

The XRD pattern of sample As(III)/Lp-*Sp* #4 (Fig. 3b) displays maxima characteristic of GR1(CO_3) mixed with those of lepidocrocite. Samples As(III)/Lp-*Sp* #5 and #6 (Fig. 3b) reveal GR1(CO_3) to be the dominant reaction product mixed with a minor amount of FCH. No evidence for lepidocrocite was found in these diffractograms, indicating its total transformation into GR1(CO_3). Finally, the XRD pattern of sample As(III)/Lp-*Sp* #7 (Fig. 3b) is dominated by broad peaks due to FCH; only the three main lines of GR1(CO_3) are still visible in this sample. A reaction time of twenty-two months was insufficient to achieve complete reduction of Fe(III) to Fe(II) in the presence of As(III). Overall, the amount of GR1(CO_3) decreased with increasing incubation time (2–22 months), while the amount of FCH increased over the time interval 5–22 months.

The RT backscattering Mössbauer spectrum of the end-product (22 months) of this bioreduction experiment, sample As(III)/Lp-*Sp* #7, can be reasonably fit with two paramagnetic quadrupole doublets D_1 and D_2 (Fig. 4). The doublet D_1 (93%) shows large hyperfine parameters (δ (isomer shift) = 1.11 mm s^{-1}, ΔE_Q (quadrupole splitting) = 2.13 mm s^{-1}) and corresponds to the two overlapping ferrous doublets of FCH (80%) and GR1(CO_3) (13%). Such differences in the quadrupole splitting values were previously observed at room temperature in a corrosion system in which hydroxycarbonate green rust was mixed with another Fe(II)-containing solid phase (Génin et al., 2002). The doublet D_2 (7%), with a small isomer shift of 0.55 mm s^{-1} and a quadrupole splitting of 0.41 mm s^{-1}, was assigned to paramagnetic Fe^{3+} in GR1(CO_3). Mössbauer analysis thus revealed that this sample consists of 20% GR1(CO_3) and 80% FCH. This result agrees with XRD analysis, which shows dominant peaks of FCH and some minor ones due to GR1(CO_3) (Fig. 3b). These results indicate that the presence of As(III) slows down the reduction of Fe(III)-bearing GR1(CO_3) into FCH by *S. putrefaciens*.

3.3.3. Bioreduction of As(V)-adsorbed lepidocrocite

The XRD pattern of the dark-orange reaction product (sample As(V)/Lp-*Sp* #8) shows the presence of unreduced lepidocrocite (γ-FeOOH) mixed with a minor new phase (indicated by the asterisk in Fig. 3c). The XRD pattern of sample As(V)/Lp-*Sp* #9 (Fig. 3c) exhibits broad peaks ascribed to FCH. The absence of lepidocrocite in sample As(V)/Lp-*Sp* #9 demonstrates the complete reduction of Fe(III) in this phase after only five months of incubation. The poor crystallinity of FCH suggests that a fraction of arsenic adsorbs on the surfaces of FCH particles during the nucleation process, thus limiting their size (Fig. 3d).

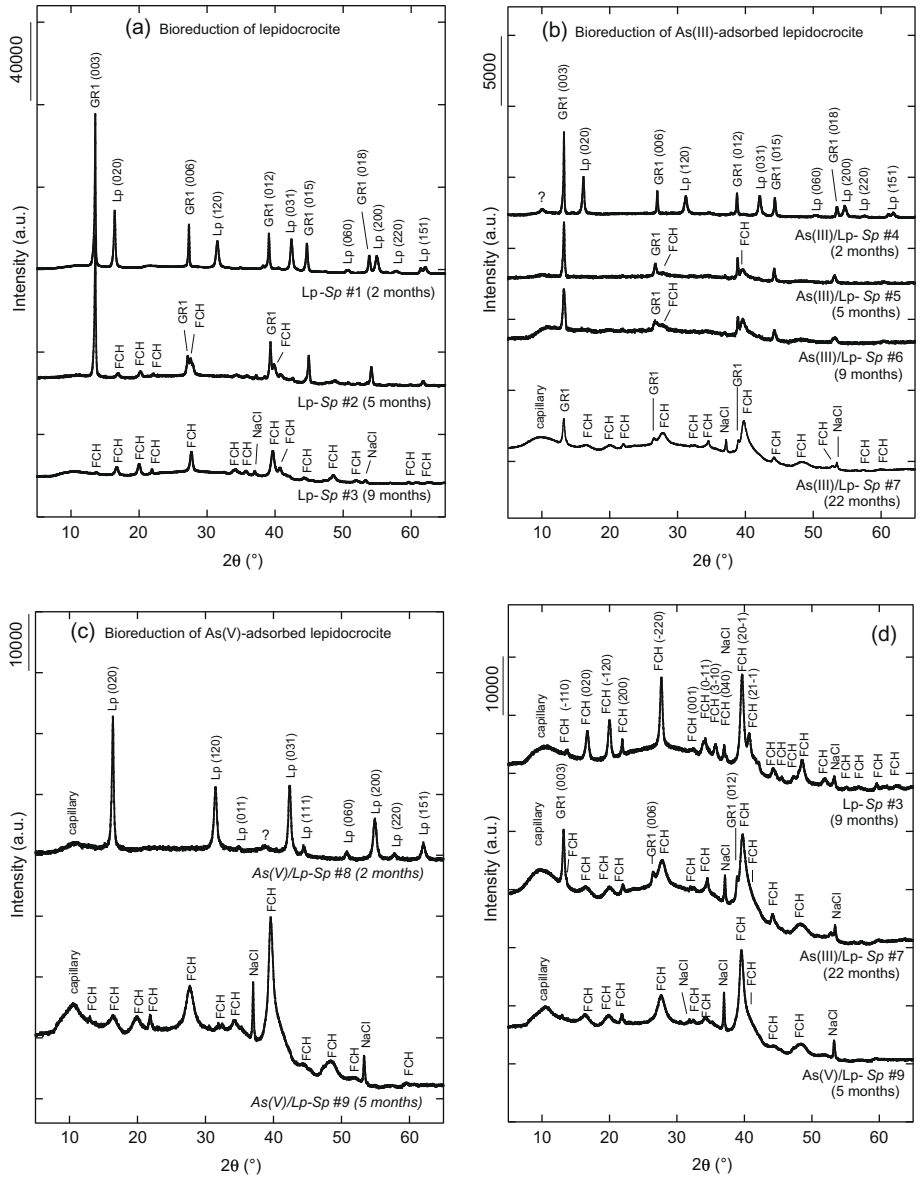

Fig. 3. X-ray powder diffraction analysis of biogenic Fe(II)-bearing compounds produced upon reduction by *S. putrefaciens* strain ATCC 12099 of (a) pure lepidocrocite, (b) As(III)-adsorbed lepidocrocite, (c) As(V)-adsorbed lepidocrocite, and (d) comparison of the final products of the bioreduction experiments. Medium 1 was used for all bioreduction experiments with ATCC 12099 (Electronic annex EA-2). Samples #1–9 correspond to different incubation times from which solid phases were harvested and vacuum-dried for analysis. GR1: hydroxycarbonate green rust 1, $Fe^{II}_4Fe^{III}_2(OH)_{12}CO_3$; FCH: ferrous-carbonate hydroxide, $Fe^{II}_2(OH)_2CO_3$; Lp: lepidocrocite, γ-FeOOH; "?" corresponds to an unknown peak. Co$K\alpha$ radiation ($\lambda = 0.179$ nm). The Bragg peaks of FCH broaden in the presence of arsenic, with similar line-width in samples #7 and #9 (d). Assuming that this broadening is mainly due to a decrease in crystallite sizes, MCD*a* and MCD*b*, calculated from the FWHM of the (200) and (020) reflections using the Scherrer formula, decrease from 47 nm and 19 nm in the absence of As (Lp-*Sp* #3), to 27 nm and 7 nm (As(III)/Lp-*Sp* #7), and 29 nm and 7 nm (As(V)/Lp-*Sp* #9) in the presence of As, respectively.

The RT backscattering Mössbauer spectrum of sample As(V)/Lp-*Sp* #9 (Fig. 4) shows two paramagnetic quadrupole doublets, D_1 and D_2, characteristic of Fe^{2+} belonging to two different phases. The doublet D_1 ($\delta = 1.15$ mm s^{-1}, $\Delta E_Q = 2.16$ mm s^{-1}) is typical of Fe(II) (87%) in FCH, while the doublet D_2 with a similar δ (1.13 mm s^{-1}) value and a larger ΔE_Q (2.82 mm s^{-1}) value is characteristic of an Fe(II) (13%) environment different from that in FCH. These Mössbauer hyperfine parameters of doublet D_2 are close to those obtained for ferrous hydroxide $Fe(OH)_2$ at room temperature by Refait et al., 1998a,b (i.e., $\delta = 1.20$ mm s^{-1}, $\Delta E_Q = 2.85$ mm s^{-1}).

TEM analysis of this end-product sample (Figs. 5 and 6) confirms the abundance of FCH with platy particles of 50–200 nm in length coated by a thick biofilm (Fig. 5a and c) associated with a minor mineral phase, which occurs as sub-spherical aggregates 50–80 nm in diameter (Fig. 5a and b). This latter phase likely corresponds to the minor

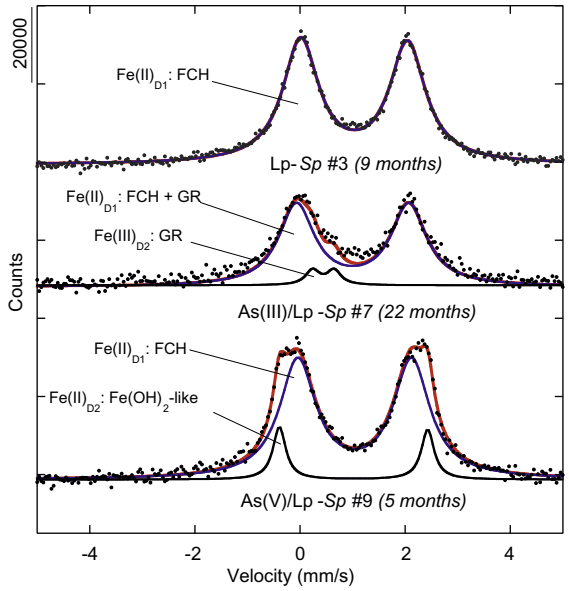

Fig. 4. Characterization of biogenic Fe(II)-containing end reaction products using backscattering Mössbauer spectroscopy at room temperature.

$Fe(OH)_2$-like phase detected by Mössbauer spectroscopy in this sample (Fig. 4). Indeed, semi-quantitative analysis of the XED spectra indicate that iron is a major element of these sub-spherical aggregates (Figs. 5b and 6e), and EELS data indicate that iron in these aggregates occurs in the Fe(II) valence state, based on comparison with EELS spectra of goethite and siderite standards (Fig. 6f). Iron is associated with high concentrations of Co and Ni in this phase (Figs. 5c and 6f), suggesting that Co^{2+} and Ni^{2+} ions present in the incubation medium (8.10^{-5} M and 8.10^{-6} M, respectively; EA-2) may substitute for Fe^{2+} ions in this $Fe(OH)_2$-like phase. In addition, arsenic is concentrated in these sub-spherical aggregates with a As/(Fe + Co + Ni) molar ratio of ~0.35(5) (Figs. 5b and 6e), whereas arsenic only occurs at low concentration in FCH with a As/Fe molar ratio of ~0.04(1) (Fig. 5c). Semi-quantitative analysis of the XED spectra indicates a slightly higher As/(Fe + Co + Ni) molar ratio in the As-rich aggregates of As(V)/Lp-*Sp* #9 (~0.35) than in the R0.3 model compound (~0.25) (Fig. 6e). Hence, despite being a minor phase, the As-rich $Fe(OH)_2$-like phase is the major arsenic host in sample As(V)/Lp-*Sp* #9. Mössbauer data indicate that FCH and the minor As-rich $Fe(OH)_2$-like phase represent 87% and 13%, respectively, of the total iron. Based on XEDS results, which indicate As/(Fe + Co + Ni) = 0.35(5) and Fe/(Fe + Co + Ni) = 0.34(5) in the As-rich $Fe(OH)_2$-like phase and As/Fe = 0.04(3) in the FCH phase, the proportion of total arsenic associated with the $Fe(OH)_2$-like phase is estimated to be 70–95% in the As(V)/Lp-*Sp* #9 sample. HRTEM analysis indicates that the As-rich sub-spherical aggregates of the $Fe(OH)_2$-like phase consist of a coherent aggregation

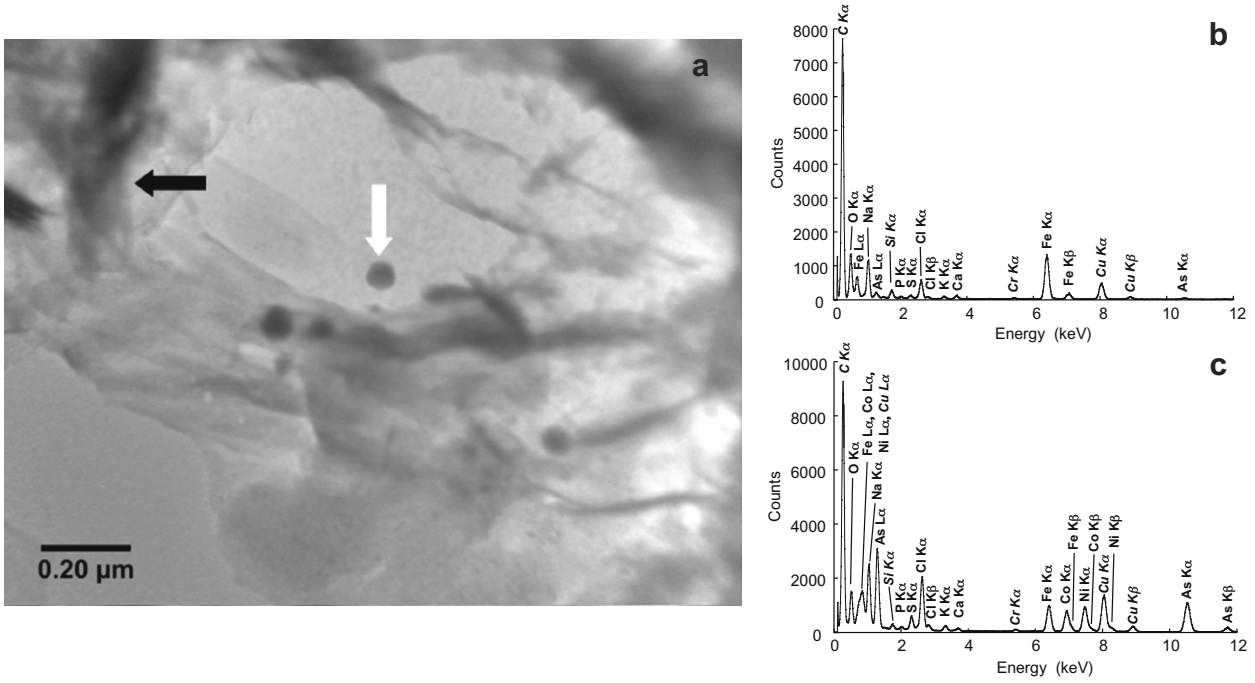

Fig. 5. TEM observation of the As/Lp-*Sp* sample following anaerobic reduction by *Shewanella putrefaciens* ATCC 12099. (a) Two mineral phases occur and are embedded in an abundant biofilm. (b) XEDS spectrum of the major phase (black arrow) identified as ferrous carbonate hydroxide by bulk XRD and Mössbauer spectroscopy, showing a small amount of associated arsenic. Estimation of molar ratios yields As/Fe = 0.039(10). (c) XEDS spectrum of a particle of the minor phase (white arrow) showing a high concentration of arsenic associated with Fe, Co, and Ni. The Cu signal is an artifact due to the fluorescence of the copper grid used as sample holder. Molar ratios estimated by averaging ~10 analyses of each component were As/(Fe + Co + Ni) = 0.35(5) and Fe(Fe + Co + Ni) = 0.34(5). A more detailed HRTEM analysis of this phase is displayed in Fig. 6.

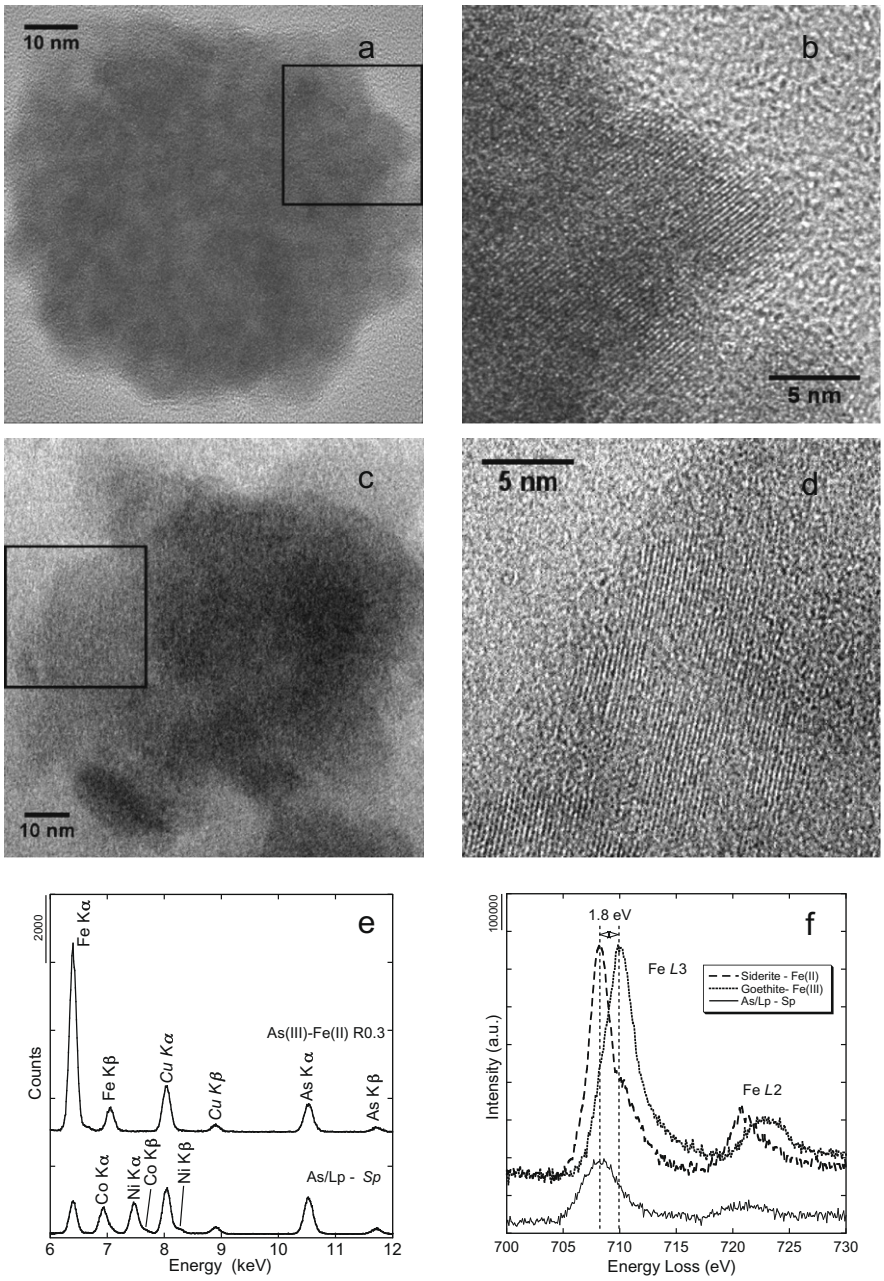

Fig. 6. Comparative HRTEM analysis of arsenic rich particles in the As(V)/Lp-*Sp* #9 sample and of the Fe(II)–As(III) model compound (R0.3). (a) HRTEM image of the As-rich particle marked by a white arrow in Fig. 5a in the biogenic sample As/Lp-*Sp*. (b) Detail of Fig. 6a (square), showing an assemblage of nano-particles. (c) HRTEM image of particles in sample Fe(II)–As(III) (R0.3). (d) Details of Fig. 6c (square) also showing an assemblage of nano-particles. (e) XED spectra of the particles in Fig. 6a and c, showing high As concentration. The Cu signal is an artifact due to the fluorescence signal of the copper grid used as sample holder. Molar ratios estimated by averaging ~10 analyses of each component were As/(Fe + Co + Ni) = 0.35(5) and Fe/(Fe + Co + Ni) = 0.34(5) for the As/Lp-*Sp* and As/Fe = 0.25(5) for R0.3 samples, respectively. Estimated standard deviations (1 s) are given in parentheses and refer to the last digit. (f) EELS Fe $L_{2,3}$ edges for a reference goethite particle with a maximum at 710.0 eV, a reference siderite particle with a maximum at 708.2 eV and the particle in the As/Lp-*Sp* sample (Fig. 6a) with a maximum at 708.2 eV, suggesting that iron is mainly present as Fe(II).

of nanocrystalline particles with diameters of 3–8 nm (Fig. 6a and b). This texture is similar to that observed in the X-ray amorphous model compound R0.3 (Fig. 6c and d). Additional characterization of these mineral phases was carried out using EXAFS spectroscopy at the Fe and As K-edge, as detailed in the following sections.

3.4. Fe K-edge EXAFS results

The Fe K-edge EXAFS spectrum of As(III)/Lp-*Sp* #7 and As(V)/Lp-*Sp* #9 was found to be similar to that of FCH (Appendix A), with characteristic second-neighbor features as well as long-distance multiple-scattering contri-

butions related to the double octahedral chain arrangement of the malachite structure (Zigan et al., 1977). These EXAFS-derived results are consistent with XRD, Mössbauer, and HRTEM results on these samples, which indicate that they consist mainly of FCH, with a minor green-rust component in As(III)/Lp-*Sp* #7 and with a minor $Fe(OH)_2$-like phase in As(V)/Lp-*Sp* #9. Owing to the poor sensitivity of EXAFS to minor phases (<10–15%), the nature of these minor phases could not be directly determined by EXAFS analysis of samples As(III)/Lp-*Sp* #7 and As(V)/Lp-*Sp* #9 at the Fe K-edge.

Fe K-edge EXAFS data were collected on the As(III)-co-precipitated Fe(II)-hydroxide model compounds (R0.1 an R0.3) in order compare the local structures of As(III) in these materials with that of $Fe(OH)_2$ (Fig. 7). Such a comparison is useful because the composition and texture of the As-rich $Fe(OH)_2$-like phase in sample As(V)/Lp-*Sp* #9 are similar to those of the R0.3 model compound (Fig. 6) and because the AsK-edge XAFS spectra of the biogenic samples are similar to those of these model compounds, as detailed in the next section (Figs. 8 and 9). Unfiltered k^3-weighted EXAFS data of the R0.1 an R0.3 model compound samples and their corresponding FT diagrams are compared with those of $Fe(OH)_2$ (brucite-type structure) in Fig. 7. The spectra are similar except for the decrease in intensity of the second- and further-neighbor contributions with increasing As-concentration. Table 2 lists the results of the fitting of the unfiltered $k^3\chi(k)$ EXAFS functions. First-neighbor contributions were fit with 3.8–4.5 oxygen atoms at 2.13–2.14 Å. Both the number of neighbors and Fe–O distance are slightly lower than those expected for Fe(II) in octahedral coordination in the $Fe(OH)_2$ crystal structure (i.e. 6 oxygen neighbors at 2.21 Å) (Table 2). Well-resolved pre-edge peaks of the three samples ($Fe(OH)_2$, R0.1 and R0.3) are similar to those of fayalite (Wilke et al., 2001), suggesting little or no Fe(III) in these samples (Electronic annex EA-3). Consequently,

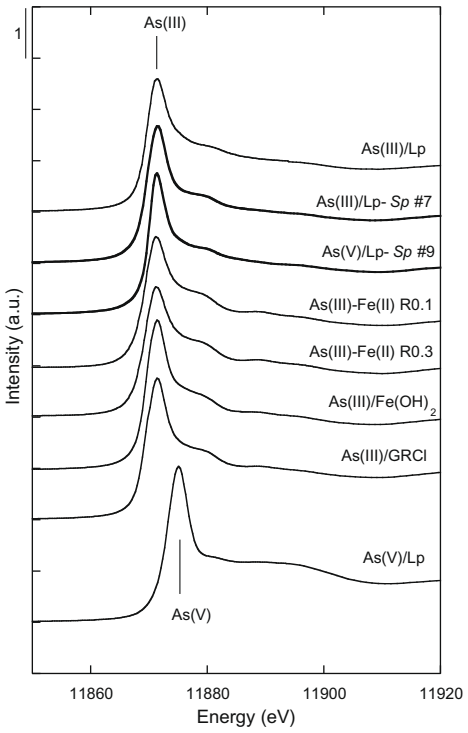

Fig. 8. Arsenic K-edge XANES spectra of the end-products of the bioreduction of As(III) and As(V)-adsorbed lepidocrocite (As(III)/Lp-*Sp* #7 and As(V)/Lp-*Sp* #9) compared with co-precipitation (R0.1 and R0.2) and sorption (As(III)/Lp, As(III)/$Fe(OH)_2$, As(III)/GRCl and As(V)/Lp) model compounds. Note that As(V) was bioreduced to As(III), whose maximum absorption are at 11,875.0 ± 0.1 eV and 11,871.3 ± 0.1 eV, respectively.

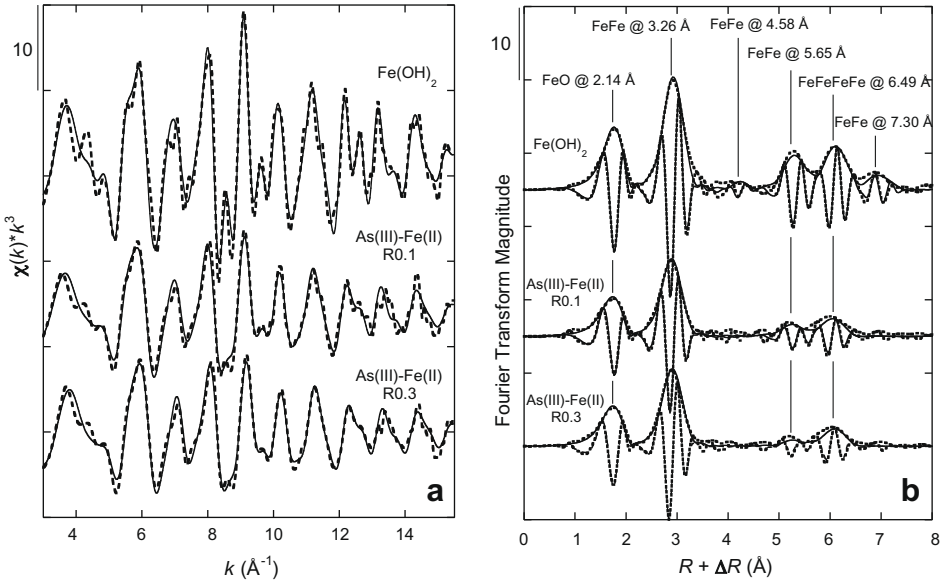

Fig. 7. Iron K-edge EXAFS data recorded at 10 K for three selected model compounds: crystalline $Fe(OH)_2$, Fe(II)–As(III) hydroxides R0.1 and R0.3 (see text). (a) k^3-weighed $\chi(k)$ EXAFS, and (b) their corresponding Fourier transforms (FT), including the magnitude and imaginary part of the FT. Experimental and calculated curves are displayed as dashed and solid lines, respectively. All fit parameters are detailed in Table 2.

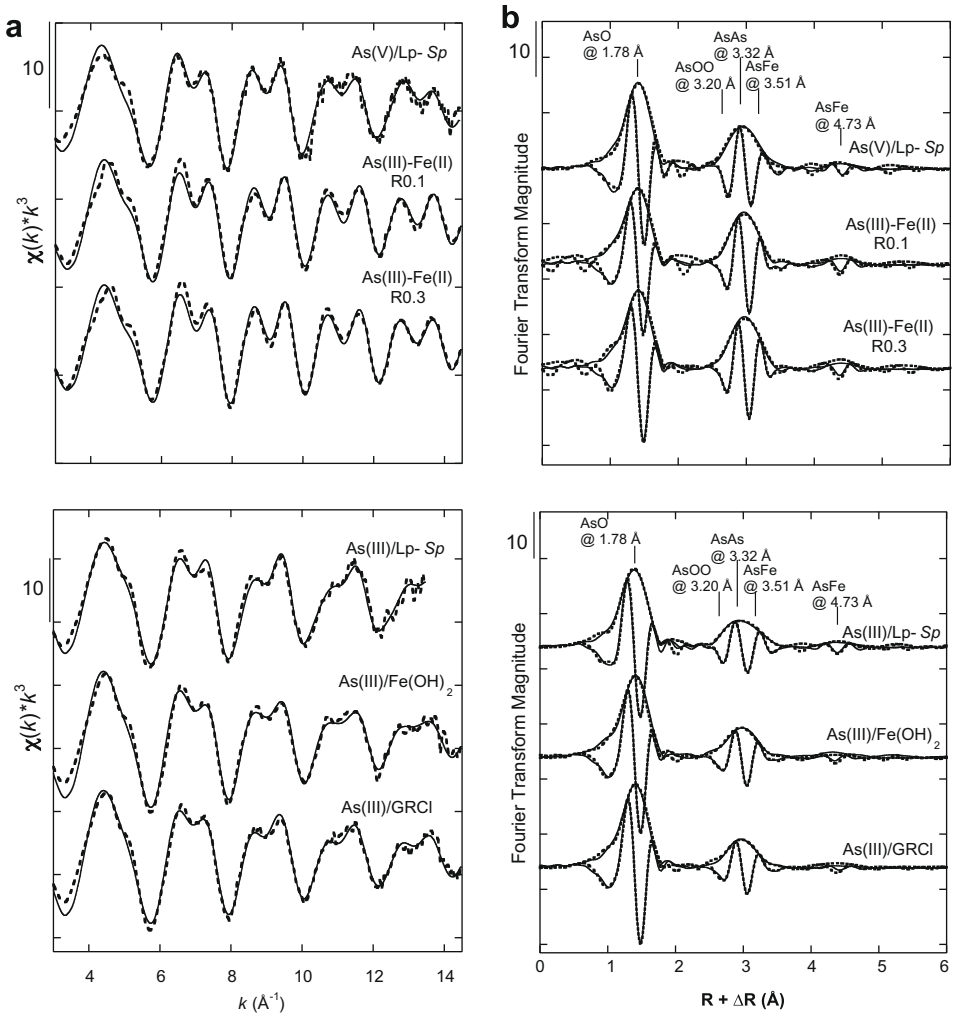

Fig. 9. Arsenic K-edge EXAFS data recorded at 10 K for the biogenic As-bearing samples and model compounds showing similarities between As(V)/Lp-*Sp* #9 and the As-rich As(III)–Fe(II) co-precipitates, and between As(III)/Lp-*Sp* #7 and the sorption samples: (a) unfiltered k^3-weighed $\chi(k)$ EXAFS, and (b) their corresponding Fourier transforms (FT), including the magnitude and imaginary part of the FT. Experimental and calculated curves are displayed as dashed and solid lines, respectively. All fit parameters are detailed in Table 3.

the difference between Fe–O distances measured by EXAFS and those derived from the crystal structure refinement of Chichagov et al. (1990) (Table 2) might be due to differences in the fractional z positions of the oxygen atom, as is known to occur for other isostructural minerals [e.g., $z = 0.23$ in portlandite, $Ca(OH)_2$ (Xu et al., 2007), whereas $z = 0.22$ in brucite, $Mg(OH)_2$ (Zigan and Rothbauer, 1967)]. The $z = 1/4$ position proposed by Chichagov et al. (1990) thus appears to be an approximation. Indeed, assuming $z = 0.23$ for $Fe(OH)_2$ yields a Fe–O distance of 2.16 Å, in agreement with that measured by EXAFS (2.14 ± 0.02 Å). The difference in the number of first neighbors falls within the classical uncertainty of the S_0^2 parameter in FEFF8, which may vary within the 0.7–1.0 range (Ankudinov et al., 1998).

The R0.1, R0.3, and $Fe(OH)_2$ samples exhibit sharp contributions from second and more distant neighbors (Fig. 7b). These contributions are weaker in R0.1 and R0.3 than in $Fe(OH)_2$. For all three samples, the dominant Fe–Fe pair correlation, observed at a distance of 3.26 ± 0.02 Å, is consistent with that expected for edge-sharing octahedra within the $Fe(OH)_2$ layer (Table 3; Fig. 7). In $Fe(OH)_2$, we observe 5.9 ± 0.5 Fe neighbors at this distance, which is consistent with the brucite-type layer structure. The number of neighbors at this distance is lower in R0.1 and R0.3 (4.4 ± 0.5) suggesting that the size of the $Fe(OH)_2$ layers is smaller in these samples than in $Fe(OH)_2$. This result is confirmed by XRD data, which suggest that R0.1 and R0.3 consist of nano-sized $Fe(OH)_2$ layers (Appendix B). Fitting of the more distant contributions indicates that they essentially arise from Fe–Fe pair correlations at a distance of 5.65 ± 0.05 Å and from Fe–Fe–Fe and Fe–Fe–Fe–Fe multiple-scattering (MS) paths at 6.45 ± 0.05 Å and 6.55 ± 0.05 Å, respectively. These distances agree with those derived from the $Fe(OH)_2$ structure (Table 2). Minor out-of-plane (Fe–Fe at 4.58 ± 0.05 Å) and

Table 2
Results of shell-by-shell fitting of unfiltered EXAFS data at Fe K-Edge for $Fe(OH)_2$ and As(III)–Fe(II) co-precipitates model compounds. The fits (Fig. 7) are consistent with the structure of $Fe(OH)_2$ (Fig. 11a). However, the diminution of the numbers of neighbors and the disappearance of the Fe–Fe distance at 4.58 Å and Fe–Fe–O multiple-scattering at 7.30 Å when As is present, indicate that samples As(III)–Fe(II) R0.1 and R0.3 consist of an As-rich nano-$Fe(OH)_2$ layered phase (Fig. 11b).

	Samples					$Fe(OH)_2$ Structure[(A)]	
	R (Å)	N	σ (Å)	ΔE_0 (eV)	CHI^2_{FT}	R (Å)	N
$Fe(OH)_2$	2.14	4.5 Fe–O	0.07	4	0.29	2.21	6 Fe–O
	3.26	5.9 Fe–Fe	0.07	–		3.26	6 Fe–Fe
	4.58	0.9 Fe–Fe	–	–		4.61	2 Fe–Fe
	5.65	8.2 Fe–Fe	–	–		5.64	18 Fe–Fe
	6.49	4.4 Fe–Fe–Fe–Fe	–	–		6.52	6 Fe–Fe
	7.30	7.8 Fe–Fe–O	–	–		6.52	18 Fe–Fe–Fe
As(III)–Fe(II) R0.1	2.13	3.7 Fe–O	0.08	2	0.19	6.52	12 Fe–Fe–Fe–Fe
	3.24	4.4 Fe–Fe	0.07	–		7.28	12 Fe–Fe
	5.63	3.1 Fe–Fe	–	–		7.3	24 Fe–Fe–O
	6.44	1.9 MS[a]	–	–			
As(III)–Fe(II) R0.3	2.13	3.8 Fe–O	0.08	5	0.16		
	3.24	4.2 Fe–Fe	0.07	–			
	5.63	1.6 Fe–Fe	–	–			
	6.44	1.8 MS[a]	–	–			

Note: R (Å): interatomic distances; N: number of neighbors; σ (Å): Debye Waller factor, ΔE_0 (eV): difference between the user-defined threshold energy and the experimentally determined threshold energy, in electron volts; Fe–Fe–Fe–Fe: multiple-scattering paths between three linear Fe atoms; Fe–Fe–O: multiple-scattering paths between two adjacent Fe atoms and one bridging O atom. During the fitting procedure, all parameter values indicated by (−) were linked to the parameter value placed above in the table. Errors on R and N values, estimated from the fit of the $Fe(OH)_2$ Fe K-edge EXAFS data, are ±0.02 and 50% below $R = 4$ Å, ±0.05 and 100% above $R = 4$ Å. Errors on σ and ΔE_0 values are ±0.01 and ±3, respectively.
[(A)] Major single and multiple-scattering paths according to Feff8 analysis of the $Fe(OH)_2$ (brucite-type) crystal structure (Chichagov et al., 1990).

in-plane (Fe–Fe and Fe–Fe–O at 7.30 ± 0.5 Å) contributions are also observed in the EXAFS data of $Fe(OH)_2$, in agreement with its crystal structure, but these pair correlations are below the detection limit in R0.1 and R0.3 (Fig. 7b, Table 2). In $Fe(OH)_2$, the number of observed neighbors for all of these long-distance contributions ranges from a half to one third of the predicted values (Table 2). These differences can be explained by EXAFS interference with other contributions from several other minor single and multiple-scattering paths that were not taken into account in our fit. Nevertheless, the number of neighbors observed for the dominant long-distance contributions is significantly lower in R0.1 and R0.3 than in $Fe(OH)_2$, supporting the nano-sized dimension of the $Fe(OH)_2$ layers in R0.1 and R0.3 (Table 2). These EXAFS results are fully consistent with the HRTEM observations, which indicate that sample R0.3 consists of aggregates of nano-crystalline particles 2–5 nm in diameter (Fig. 6d). The similar texture observed by HRTEM in the spherical As-rich aggregates from As(V)/Lp-*Sp* (Fig. 6b) suggests that these As-rich particles consist of nano-sized layers with the $Fe(OH)_2$ structure; they are the same as those identified as a minor phase by Mössbauer spectroscopy (Fig. 4). In addition, TEM-XEDS data suggest that Co^{2+} and Ni^{2+} substitute for Fe^{2+} in these layers (Fig. 6e).

3.5. Arsenic oxidation state

Arsenic K-edge XANES spectroscopy was used to determine the oxidation state of As in the samples. The XANES spectra of As(V)-adsorbed lepidocrocite and As(III)-adsorbed lepidocrocite samples exhibit well-resolved edge structures with absorption maxima at 11,875.0 eV and 11,871.3 eV (Fig. 8), which correspond to the K-edge energies of $HAs(V)O_4^{2-}$ and $H_3As(III)O_3$, respectively (Morin et al., 2003). These samples were used in the present study as abiotic controls of arsenic oxidation state, and showed that As(V) and As(III) were not reduced or oxidized during their interactions with lepidocrocite after one week of incubation without bacteria. This observation is consistent with previous abiotic studies which showed that As(V) or As(III) does not reduce or oxidize, respectively, in the presence of ferrihydrite (Ona-Nguema et al., 2005), goethite (Farquhar et al., 2002; Manning et al., 2002; Ona-Nguema et al., 2005), maghemite (Morin et al., 2008), or lepidocrocite (Farquhar et al., 2002; Manning et al., 2002; Ona-Nguema et al., 2005) even after one week of equilibration time under anoxic conditions (Ona-Nguema et al., 2005).

In contrast, the XANES spectrum of sample As(V)/Lp-*Sp* #9, obtained after bacterial reduction of As(V)-adsorbed lepidocrocite, exhibits an absorption maximum at 11,871.3 eV (Fig. 8). Moreover, As(III) did not oxidize during its interactions with *S. putrefaciens*. This result indicates that *S. putrefaciens* strain ATCC 12099 is capable of reducing adsorbed As(V) on the lepidocrocite surfaces. No As(III) oxidation was observed in sample As(III)/Lp-*Sp* #7, in which strain ATCC 12099 reduced Fe(III) in As(III)-adsorbed lepidocrocite and GR1(CO_3), forming FCH (Fig. 8).

Table 3
Results of shell-by-shell fitting of unfiltered EXAFS data at As K-Edge. The fits (Fig. 9) are consistent with the major occurrence of multinuclear As(III) complexes onto Fe trioctahedral layers in all samples (see text, Fig. 11).

Sample	R (Å) (±0.02)	N (±0.5)	σ (Å) (±0.01)	ΔE_0 (eV) (±3)	CHI^2_{FT}
As(V)/Lp-*Sp* #9	1.78	2.9 As–O	0.06	11	0.17
	3.20 (f)	6.0 (f) As–O–O	–	–	
	3.32	1.6 As–As	0.05	–	
	3.5	1.5 As–Fe	–	–	
	4.76	0.5 As–Fe	–	–	
As(III)–Fe(II) R0.1	1.78	2.9 As–O	0.07	16	0.17
	3.20 (f)	6.0 (f) As–O–O	–	–	
	3.32	2.6 As–As	0.06	–	
	3.51	1.3 As–Fe	–	–	
	4.73	0.7 As–Fe	–	–	
As(III)–Fe(II) R0.3	1.79	2.7 As–O	0.06	16	0.16
	3.20 (f)	6.0 (f) As–O–O	–	–	
	3.32	2.7 As–As	0.06	–	
	3.51	1.0 As–Fe	–	–	
	4.72	0.7 As–Fe	–	–	
As(III)/$Fe(OH)_2$	1.78	3.0 As–O	0.06	16	0.09
	3.21	6.0 (f) As–O–O	–	–	
	3.32	1.9 As–As	0.07	–	
	3.51	0.9 As–Fe	–	–	
	4.69	0.5 As–Fe	–	–	
As(III)/GRCl	1.78	2.9 As–O	0.06	16	0.09
	3.22	6.0 (f) As–O–O	–	–	
	3.32	1.2 As–As	0.05	–	
	3.5	0.8 As–Fe	–	–	
	4.72	0.3 As–Fe	–	–	
As(III)/Lp-*Sp* #7	1.77	2.5 As–O	0.05	16	0.09
	3.20 (f)	6.0 (f) As–O–O	–	–	
	3.31	1.1 As–As	0.06	–	
	3.48	1.0 As–Fe	–	–	
	4.74	0.7 As–Fe	–	–	

Note: R (Å): interatomic distances; N: number of neighbors; σ (Å): Debye Waller factor, ΔE_0 (eV): difference between the user-defined threshold energy and the experimentally determined threshold energy, in electron volts; CHI^2_{FT}: Goodness of fit (see text). Including the As–O–O multiple-scattering paths improved the fits but did not change the results on other shells, with respect to our estimated errors. During the fitting procedure, all parameter values indicated by (−) were linked to the parameter value placed above in the table. Errors on R and N values, estimated from the fit of the tooeleite As K-edge EXAFS data (not shown), are ±0.02 and ±0.5. Errors on σ and ΔE_0 values are ±0.01 and ±3, respectively.

3.6. Arsenic K-edge EXAFS results: local environment of arsenic

Arsenic K-edge XANES spectra of the Fe(II)–As(III) co-precipitates and adsorption model compounds exhibit similar shapes, while those of As(V)/Lp-*Sp* #9 and As(III)/Lp-*Sp* #7 are less structured (Fig. 8). This difference suggests that arsenic speciation in these biogenic samples differs slightly from that in the model compounds. Unfiltered k^3-weighted As K-edge EXAFS data from the samples studied and their corresponding Fourier Transforms are displayed in Fig. 9. In contrast with the slight differences observed in the As K-edge XANES spectra, all As K-edge EXAFS spectra exhibit strong similarities, although the second-neighbor contributions are less intense for the As(III)/Lp-*Sp* #7 sample and the sorption samples, As(III)/$Fe(OH)_2$, and As(III)/GR1(Cl) than for As(V)/Lp-*Sp* #9 sample and the R0.1, R0.3 model compounds. Table 3 lists the results of fitting the unfiltered $k^3\chi(k)$ EXAFS functions. The first-neighbor contribution was fit with 2.5–3.0 oxygen atoms at 1.77–1.79 Å corresponding to an $As^{III}O_3$ pyramid. A multiple-scattering contribution corresponding to the six As–O–O–As paths within the $As^{III}O_3$ pyramid was included in the fit, with the number of paths fixed at the expected value of 6. The path-length fit for this contribution (3.15–3.20 Å) is close to that expected from the structure of arsenolite (Ballirano and Maras, 2002).

For all samples, the sharp second-neighbor contribution is best fit by a dominant As–As pair at a distance of 3.32 ± 0.02 Å. The number of As neighbors at this distance in the biogenic samples As(V)/Lp-*Sp* (1.6 ± 0.5) and As(III)/Lp-*Sp* (1.1 ± 0.5) is closer to that in the sorption samples (1.9 ± 0.5 and 1.2 ± 0.5 for As(III)/$Fe(OH)_2$ and As(III)/GR1(Cl), respectively) than to that in R0.1 and

R0.3 (2.5 ± 0.5) (Table 3). An additional As–Fe pair correlation at a distance of 3.50 ± 0.02 Å with 1.0 ± 0.5 neighbor significantly improved the fits for all samples and decreased the reduced CHI^2 and CHI^2_{FT} values by almost a factor of two (Electronic annex EA-4).

Importantly, attempts to fit the ~3.3 Å distance with an As–Fe pair correlation, including (or not including) the additional As–Fe pair correlation at ~3.5 Å, led to poorer fits for all samples (the reduced CHI^2 increased by 30%) and to unrealistic σ values (below 0.03 Å), indicating second-neighbor atoms heavier than Fe located at ~3.3 Å (see EA-4). The As–As distance of 3.32 ± 0.02 Å is similar to that in As–As pairs of corner-sharing AsO_3 pyramids in the iron arsenite mineral schneiderhönite (3.33 ± 0.03 Å; Hawthorne 1985), although it is slightly longer than As–As distances in other arsenite minerals such as arsenolite As_2O_3 (3.22 Å; Ballirano and Maras, 2002), fetiasite (3.25 Å; Graeser et al. 1994), and ludlockite $Pb(Fe^{3+})_4(As^{3+})_{10}O_{22}$ (3.18 ± 0.2 Å; Cooper and Hawthorne 1996).

In addition, both R0.1 and R0.3 exhibit a contribution at a longer distance in the FT of the EXAFS (Fig. 9b), that could be fit with ~2 Fe atoms at a distance of 4.75 Å. This contribution is weak in the EXAFS FT's of the sorption samples As(III)/$Fe(OH)_2$ and As(III)/GR1(Cl) and of the As(V)/Lp-*Sp* #9 and As(III)/Lp-*Sp* #7.

4. DISCUSSION

4.1. Dissimilatory arsenate reduction

Our study presents evidence that the iron-respiring bacterium *S. putrefaciens* strain ATCC 12099 is capable of utilizing aqueous arsenate as the sole electron acceptor in the presence of methanoate as the electron source to produce As(III) in batch systems. The As(V) reduction observed in the present study does not result from a fermentation process because *S. putrefaciens* is a non-fermenting microorganism (Venkateswaran et al., 1999). Moreover, our results indicate that *S. putrefaciens* strain ATCC 12099 is also able to reduce arsenate from the As(V)-adsorbed lepidocrocite sample, as well as Fe(III) in lepidocrocite to form a solid product containing As(III) and Fe(II) mixed with an FCH phase. Indeed, arsenic K-edge XANES results indicate that all As(V) is reduced to As(III) during the biomineralization of FCH. The ability of *S. putrefaciens* strain ATCC 12099 to reduce As(V) is in agreement with a recent observation of As(V) reduction by *S. putrefaciens* strain CN-32 in flow-through column experiments (Kocar et al., 2006). In this earlier study, As(III) was the only arsenic species detected in the porewater and was the dominant arsenic species present in the solid phase upon column breakdown. Similarly, Campbell et al. (2006) recently pointed out that incubations with *Shewanella* sp. ANA-3 or with fresh sediment from Haiwee Reservoir (Olancha, CA) were capable of reducing As(V) simultaneously with, or prior to, Fe(III) reduction in hydrous ferric oxide. In addition, Zobrist et al. (2000) found that *Sulfurospirillum barnesii*, a bacterium that respires both As(V) and Fe(III), can reduce As(V) adsorbed onto ferrihydrite and As(V) adsorbed onto aluminum hydroxide as well as Fe(III) in ferrihydrite to Fe(II). These microbial processes involving the reduction of As(V) and Fe(III)-(oxyhydr)oxides could thus strongly influence the redox cycling and arsenic distribution between solid and aqueous phases in anoxic soils, sediments, and aquifers.

4.2. Bacterial reduction of hydroxycarbonate green rust 1

Green rusts are Fe(II,III) layered double hydroxides that are intermediate compounds between Fe(II)-hydroxides and Fe(III)-(oxyhydr)oxides; their structure consists of positively charged layers of composition $[Fe^{2+}_{(1-x)}Fe^{3+}_{x}(OH)_2]^{x+}$, which alternate with $[(x/n)A^{n-}\cdot(mx/n)H_2O]^{x-}$ negatively charged interlayers that include *m* water molecules per A^{n-} anion (Génin et al., 1998). According to the nature of the intercalated anion, various green rusts have been obtained under abiotic conditions, including GR1(CO_3) (e.g., Drissi et al., 1995; Benali et al., 2001; Legrand et al., 2001), hydroxychloride green rust 1 GR1(Cl) (Refait and Génin, 1993), hydroxyformate green rust 1 GR1(HCO_2) (Refait et al., 2006), hydroxysulphite green rust 1 GR1(SO_3) (Simon et al., 1997), hydroxyoxalate green rust 1 GR1(C_2O_4) (Refait et al., 1998a, b), and hydroxysulphate green rust 2 GR2(SO_4) (e.g., Hansen et al., 1994; Genin et al., 1996; Refait et al., 2003; Simon et al., 2003). Green rust has been identified as the mineral fougerite in reductomorphic soils (Trolard et al., 1997; Refait et al., 2001; Trolard et al., 2007) where it plays a central role in the geochemistry of iron by controlling the concentration of dissolved Fe(II) ions in aqueous solutions (Bourrié et al., 1999). The nature of the interlayer anion in fougerite depends on the environment of formation. GR1(CO_3) is often obtained under reducing conditions as the result of the activity of IRBs from the reduction of Fe(III) in ferrihydrite (Parmar et al., 2001; Zachara et al., 2002; Glasauer et al., 2003; Kukkadapu et al., 2004), or lepidocrocite (Ona-Nguema et al., 2001, 2002a, b, 2004; O'Loughlin et al., 2007).

In the studies cited above, Fe(III)-oxyhydroxides were used as the terminal electron acceptor, and GR1(CO_3) was considered to be either an intermediate compound for magnetite formation or the end reaction product. The formation of magnetite via dissolution of green rust is not the result of bacterial activity as demonstrated by Ona-Nguema et al. (2002a). None of these studies have shown the ability of IRBs to reduce iron in green rust. Recently, Zegeye et al. (2007) used a sulphate-reducing bacterium (SRB), *Desulfovibrio alaskensis*, to reduce an abiogenic GR2(SO_4) and a biogenic GR2(SO_4) mixed with a minor amount of lepidocrocite. This biogenic GR2(SO_4) was obtained from the reduction of lepidocrocite by *S. putrefaciens* in the presence of H_2 as the electron source as described by Zegeye et al. (2005). In the study by Zegeye et al. (2007), SRB cells used both abiogenic and biogenic GR2(SO_4) as sulphate sources to form a mixture of GR1(CO_3), vivianite, and greigite. Our results provide the first evidence of bacterial reduction of Fe(III) in GR1(CO_3) by an IRB, *S. putrefaciens* strain ATCC 12099, that leads to the formation of FCH in the presence or absence of As(III). These results confirm the central role of green rusts in the pathways of the formation of Fe-oxyhydroxides or Fe-hydroxides in oxic–anoxic boundary regions or in anoxic environments, respectively.

4.3. Ferrous-carbonate hydroxide formation

Ferrous carbonate hydroxide [$Fe^{II}_2(OH)_2CO_3$: FCH] was the only crystalline phase detected by XRD in the end bioreduction product of pure lepidocrocite and As(V)-adsorbed lepidocrocite. It was also the major crystalline phase in association with green-rust in the end bioreduction product of As(III)-adsorbed lepidocrocite. FCH is a rosasite-type basic carbonate, and this mineral class includes the well-known phase malachite [$Cu(OH)_2CO_3$] (Zigan et al., 1977). Kukkadapu et al. (2005) provided the first evidence for the formation of FCH under Fe-reducing conditions from the reduction of biogenic cation-excess magnetite by *S. putrefaciens* strain CN-32 after a long-term incubation (22 months). This earlier study implied that the kinetics of FCH formation is slow and that active iron-respiring bacteria are not necessarily required. Our results are consistent with these observations and show that the kinetics of biogenic FCH formation varies, depending on the specific system (Fig. 10, pathways A–C). FCH can readily form (within five months) when both Fe(III) and As(V) serve as electron acceptors in the same medium as in the case of As(V)-adsorbed lepidocrocite (pathway A, Fig. 10). We suggest that pathway A takes place in two steps, the first of which involves the reduction of Fe(III) in lepidocrocite into Fe(II) ions by strain ATCC 12099, leading to the formation of an amorphous As(V)-bearing Fe(II,III)-hydroxide phase instead of the GR1(CO_3) observed for pure lepidocrocite or As(III)-sorbed lepidocrocite (pathways B and C). Adsorbed arsenate is indeed known to poison the growth of iron oxides and hydroxides (e.g., Waychunas et al., 1996). The second step involves the rapid reduction of this amorphous phase, including the reduction of As(V) to As(III), leading to the formation of a mixture of FCH and an amorphous As(III)-bearing Fe(II)-hydroxide phase. The reasoning behind this suggestion is that no intermediate phase consisting of lepidocrocite or GR1(CO_3) with sorbed As(III) is observed in pathway A, which might be the case if the reduction of arsenic preceded the reduction of Fe(III). The acceleration of the reaction in this case, compared to pathways B and C, might be related to the higher solubility of the putative amorphous As(V)-bearing Fe(II,III)-hydroxide phase, compared to GR1(CO_3). FCH is produced in 8–9 months from pure lepidocrocite reduction (pathway B), whereas it is still mixed with GR1(CO_3) after 22 months in the system in which As(III)-adsorbed lepidocrocite was the electron acceptor (pathway C, Fig. 10). This result suggests that As(III) does not hinder the formation of GR1(CO_3) at the As(III) concentration used in this study but it slows the bioreduction of Fe(III) leading to the formation FCH. Thus, the rate of Fe(III) reduction increases in the order: As(V)-adsorbed lepidocrocite > pure lepidocrocite > As(III)-adsorbed lepidocrocite.

4.4. Evidence for multinuclear arsenite complexes at the edges of layered $Fe(OH)_2$ nano-particles

HRTEM, XRD, and Fe K-edge EXAFS results demonstrate that the co-precipitated Fe(II)–As(III) hydroxide model compounds R0.1 and R0.3 prepared with As/Fe solution ratios of 0.1 and 0.3, consist of nano-sized $Fe(OH)_2$ layer-structured particles that are 2–5 nm in diameter (Figs. 6 and 11a). Arsenic K-edge EXAFS data indicate that arsenite adsorbs on the edges of these nano-particles during the co-precipitation process. XRD results indicate that arsenic inhibits the growth of these $Fe(OH)_2$ layers as well as their stacking along the *c* direction (Appendix B). Similar observations of nano-sized $Fe(OH)_2$ layers associated with the As-rich particles in the product of the bioreduction of As(V)-doped lepidocrocite suggest that such nano-sized $Fe(OH)_2$ layers may contribute to the immobilization of arsenite after reduction of iron minerals in these samples. Moereover, adsorption of As(III) on nano-$Fe(OH)_2$ is consistent with the HRTEM and Mössbauer data on sample As(V)/Lp-*Sp* #9, which indicate the presence of an As-rich (Fe,Ni,Co)$(OH)_2$ nano-phase, coexisting with the major ferrous carbonate hydroxide phase (FCH). Such nano-phases were not detected by Mössbauer analysis of the As(III)/Lp-*Sp* #7 sample, and additional HRTEM analyses on this latter sample would be needed to potentially identify them. Nevertheless, As-EXAFS data for the As(III)/Lp-*Sp* sample can be interpreted as indicating dominant adsorption of As(III) on GR1(CO_3). Such adsorption might decrease the solubility of this phase, which could explain the slower rates of reduction to FCH in the As(III)-sorbed lepidocrocite experiment (pathway C, Fig. 10).

Our EXAFS results provide further information on the nature of this sorption processes and indicate that As(III) surface complexes have similar characteristic bonding geometries in samples As(V)/Lp-*Sp* #9 and As(III)/Lp-*Sp* #7, as well as in our Fe(II)–As(III) co-precipitation and adsorption model compounds. The observed arsenite species are characterized by As–As pair correlations at a distance of 3.32 ± 0.02 Å and by As–Fe pair correlations at a distance of 3.50 ± 0.02 Å. First the low number of As–Fe pairs at ~3.5 Å observed for all samples ($N = 0.9$–1.5) rules out the possibility of ^{3}C As(III) surface complexes above Fe vacancies in the $Fe(OH)_2$ layers. In such complexes, which were recently observed for As(III) sorption on magnetite (Wang et al., 2008), the expected *N* value is 6 and the observed *N* value is larger than 2.5. In contrast, the occurrence of As–As pair correlations indicates the formation of multinuclear arsenite species. The occurrence of As–Fe pair correlations at a distance of 3.50 ± 0.02 Å indicates that these oligomers bind to the $Fe(OH)_2$ layers by sharing corners with FeO_6 octahedra. This geometry is supported by the close match between the As–As distance (~3.3 Å) and the O–O distance (3.26 Å) along an edge of a FeO_6 octahedron in the $Fe(OH)_2$ structure. Possible models of multinuclear arsenite surface complexes consistent with our EXAFS data are displayed in Fig. 11a and b for sorption and co-precipitation samples, respectively. The observation of As–Fe pair correlations at a distance of ~4.7 Å that can be assigned to third neighbors on the edges of the $Fe(OH)_2$ layer provides strong support for these structural models. In the As(III)/$Fe(OH)_2$ and As(III)/GR1(Cl) sorption samples, the *N* value of 1.2–1.9 As atoms for the As–As pair suggests the formation of As_2O_5 dimers ($N = 1$), that can be adjacent to each other ($N = 2$). The

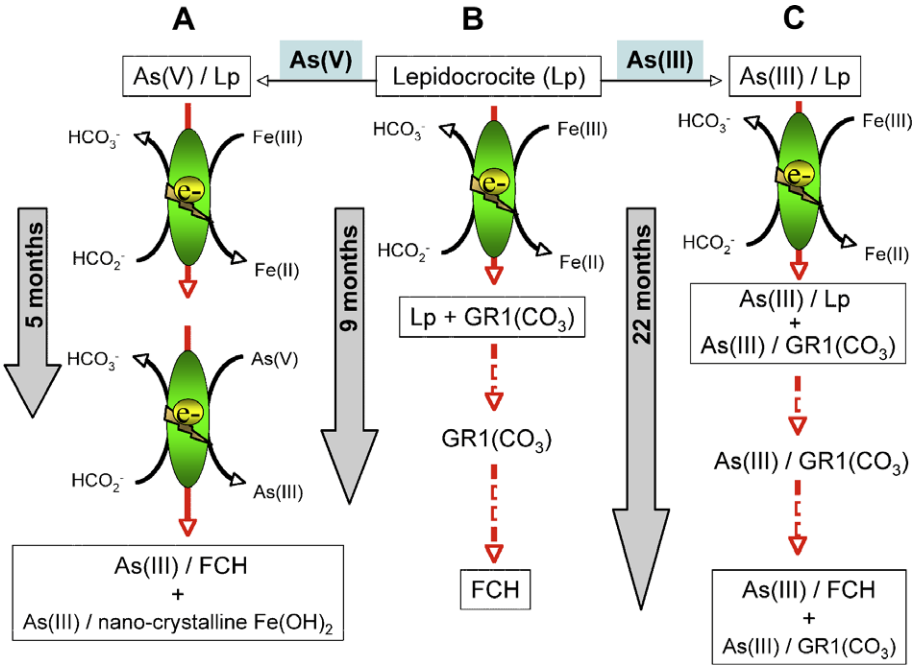

Fig. 10. Pathways of the formation of biogenic ferrous-carbonate hydroxide (FCH). Pathway A involves the reduction of both Fe(III) and As(V) in As(V)-adsorbed lepidocrocite, possibly in two steps, with reduction of Fe(III) to Fe(II) preceding the reduction of As(V) to As(III), and results in the formation of FCH and a nano-crystalline phase of Fe(II)-hydroxide with adsorbed As(III) in five months. No green rust was observed in this pathway. In pathway B, pure lepidocrocite is bacterially transformed to hydroxycarbonate green rust 1 [$GR1(CO_3)$], which is completely reduced in eight or nine months into FCH. Pathway C involves the reduction of As(III)-adsorbed lepidocrocite into $GR1(CO_3)$, which is slowly reduced to form FCH. Based on XRD and Mössbauer results, this sample still contains a minor fraction of $GR1(CO_3)$ mixed with a dominant FCH phase after 22 months of incubation. (For interpretation of the references to color in this figure legend, the reader is referred to the web version of this paper.)

higher number of As–As pair correlations in the R0.1 and R0.3 samples ($N = 2.6$–2.7 As atoms), for which the As/Fe ratio is higher than that for the sorption samples, is interpreted as the formation of arsenite polymers bonding to the $Fe(OH)_2$ layers. Fig. 11b displays a possible model consistent with these observations, in which As_nO_{2n+1} polymers form chains that are bonded to the edges of $Fe(OH)_2$ nanolayers. Restriction of such bonding to the edge of the layers is proposed because the 3-fold coordinated OH groups located in the inner region of the layer surface are expected to be less reactive than the 2-fold and 1-fold coordinated OH groups located on the edges of the layers. The proposed structure, in which arsenite chains bond to the top (and bottom) of the $Fe(OH)_2$ layer (Fig. 11b), is constrained by the O–As–O angle of ~100° in the AsO_3 pyramid, which hinders the formation of in-plane linear chains at the edge of the particles (Fig. 11a). The proposed structure yields a consistent explanation for the poisoning of $Fe(OH)_2$ layer growth and also for the dramatic loss of layer stacking observed by XRD in the R0.1 and R0.3 co-precipitation samples (Appendix B).

As discussed above, the present study provides the first evidence for such multinuclear arsenite surface complexes. Previous studies on arsenite sorption on iron oxyhydroxides and oxides reported the occurrence of arsenite surface complexes involving single AsO_3 groups, forming edge-sharing bidentate complexes (^2E), corner-sharing bidentate complexes (^2C), corner-sharing monodentate complexes (^2C) (see, e.g., Ona-Nguema et al., 2005 and references therein), and more recently corner-sharing tridentate (^3C) complexes at the surface of magnetite (Wang et al., 2008).

In a previous study, Thoral et al. (2005) reported the formation of As(III) inner-sphere complexes on Fe(II) hydroxide particles, which were produced by hydrolyzing a mixture of dissolved Fe(II) and As(III) at pH 7. On the basis of room temperature EXAFS data, an As–Fe distance at 3.30 ± 0.02 Å was interpreted as indicative of a ^2C bidentate complex, although such complexes are generally characterized by As–Fe pairs at a distance of ~3.4 Å (see, e.g., Ona-Nguema et al., 2005 and references therein). In contrast, in the present study the contribution at ~3.3 Å in the As K-EXAFS data of our As(III)–Fe(II) co-precipitation and sorption samples was best fit by an As–As pair correlation and could not be fit with an As–Fe pair correlation (see Section 3 and Electronic annex EA-4). Moreover, an additional As–Fe pair correlation at a distance of 3.5 ± 0.03 Å was necessary to fit the data properly. This difference with respect to the results of Thoral et al. (2005) on similar compounds might be explained by the fact that our EXAFS data were recorded at 10 K and over a wider k-range (14.5 $Å^{-1}$) which allowed us to better determine the shape of the amplitude of the backscattering function arising from the second-neighbors around the central As atom.

The formation of multinuclear arsenite complexes at the surface of Fe(II)-bearing layered minerals contrasts with the ^2E and ^2C complexes commonly observed at the surface of

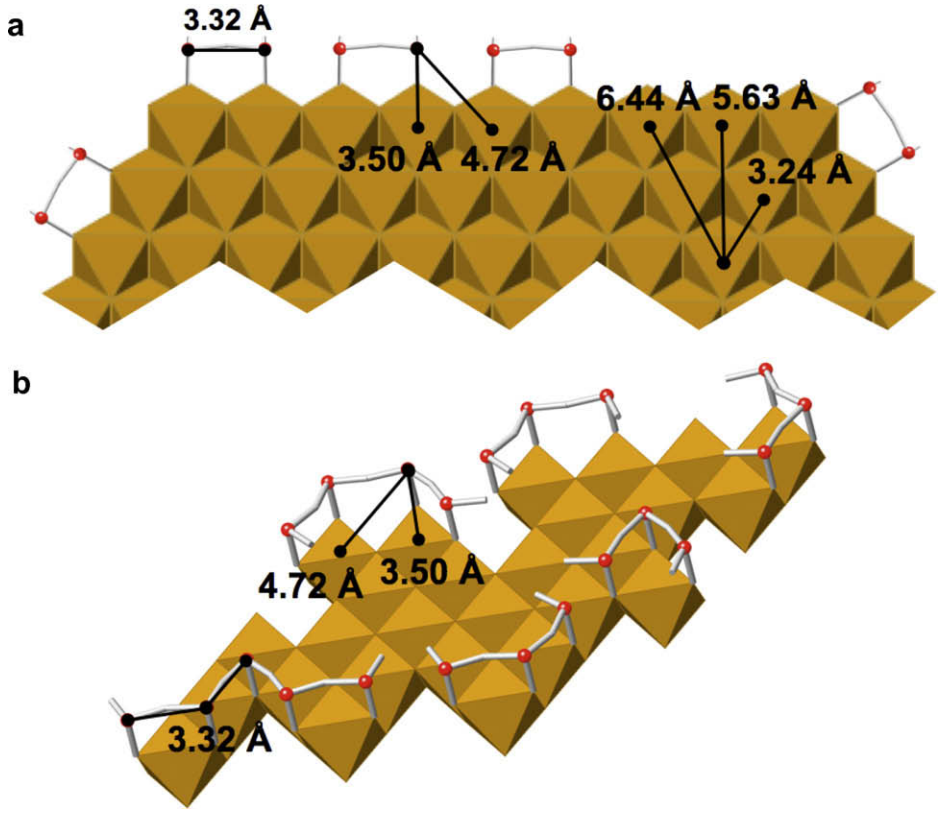

Fig. 11. Proposed structural model for (a) As(III) adsorption on the edges of green-rust or $Fe(OH)_2$ particles (b) As-rich particles in the As(V)/Lp-*Sp* #9 sample and the Fe(II)–As(III) hydroxides used as model compounds (R0.1 and R0.3). (a) The trioctahedral structure of the $Fe(OH)_2$ layer yields Fe–Fe distances of 3.24 Å, 5.63 Å, 6.44 Å and intense multiple-scattering contributions at 6.44 Å observed in the Fe K-edge EXAFS in the model compound samples (Table 2). $As^{III}{}_2O_5$ pairs bond to $Fe^{II}O_6$ octahedra at the edges of the $Fe(OH)_2$ layers via mododentate corner-sharing complex. In the sorption samples, the As atom (small red sphere) is surrounded by 1 As atom at a distance of ~3.3 Å or by 2 As atoms when two pairs are adjacent, by 1 Fe atoms at a distance of ~3.5 Å, and by 2 Fe atoms at a distance of ~4.7 Å. (b) In co-precipitation samples As_nO_{2n+1} polymers form short chains sorbed above (an below, not shown) the edges of $Fe(OH)_2$ nano-particles. Each As atom is surrounded by 1–4 As atoms ($N = 2.7$ in average in this figure) at a distance of ~3.3 Å, by 1 Fe atoms at a distance of ~3.5 Å, and by 1–2 Fe atoms at a distance of ~4.7 Å. In the As/Lp-*Sp* sample, a significant amount of Co^{2+} and Ni^{2+} likely substitute for Fe^{2+} ions in the octahedral layer (Fig. 6e). These models are consistent with our EXAFS result at the As K-edge (see text and Table 3). (For interpretation of color mentioned in this figure the reader is referred to the web version of the article.)

Fe(III) oxyhydroxides (see, e.g., Ona-Nguema et al., 2005 and references therein) and is consistent with the geometry of bonding of arsenite groups in minerals. Multinuclear arsenite groups bonded to $Fe(II)O_6$ octahedra are commonly observed in ferrous arsenite minerals such as fetiasite $Fe^{2+}{}_{1.8}Fe^{3+}{}_{0.9}Ti_{0.3}O_2As_2O_5$ (Graeser et al., 1994), schneiderhöhnite $Fe^{2+}Fe^{3+}3As_5O_{13}$ (Hawthorne, 1985), and ludlockite $Fe^{2+}{}_{0.95}Pb_{0.05}As_2O_6$ (Cooper and Hawthorne, 1996), while single arsenite pyramids can share an edge with $Fe(III)O_6$ octahedra via singly coordinated oxygen atoms in the ferric arsenite tooeleite (Morin et al., 2007).

4.5. Other arsenic species in the bioreduction products of As-sorbed lepidocrocite

Although arsenic K-edge EXAFS and HRTEM results indicate that arsenite mainly occurs in the form of multinuclear arsenite surface complexes at the edges of Fe-hydroxide layers in the bioreduction product of As-sorbed lepidocrocite, detailed analyses of the EXAFS and HRTEM–XEDS data suggest that the speciation of arsenic is more complex in the biogenic sample than in our R0.1 and R0.3 model compounds.

Indeed, XEDS analyses of As(V)/Lp-*Sp* #9 show that some As is also associated, to a lesser extent, with FCH particles. This association implies that, in addition to multinuclear arsenite surface complexes on nano-sized $Fe(OH)_2$ layers (sample As(V)/Lp-*Sp* #9) or $GR1(CO_3)$ layers (sample As(III)/Lp-*Sp* #7), other arsenite species occur in these biogenic samples. The occurrence of such species may explain why the XANES spectra of As(III)/Lp-*Sp* and As(III)/Lp-*Sp* differ from those of the Fe(II)–As(III) model compounds. The smaller mean coherent dimension of the FCH in the As/Lp-*Sp* bioassays than in the As-free one can thus be interpreted as being due to sorption of arsenite on the surface of the FCH particles. The nature of such arsenite surface complexes is difficult to predict because the morphology of the FCH particles could not be easily determined from our HRTEM observations, and the surface terminations of this phase in water are unknown.

The structure of FCH, which is similar to that of malachite (Zigan et al., 1977), exhibits infinite $Fe^{2+}O_6$ octahedral double chains that could serve as potential biding sites for arsenite, somewhat similar to those on the edges of $Fe(OH)_2$ layers. The higher number of neighbors observed for the As–Fe pair at ~3.5 Å and the lower number of neighbors for the As–As pair at ~3.3 Å, compared to the model compound samples (Table 2), can be interpreted as being due to the presence of additional monodentate ^1V complexes at the surfaces of FCH particles.

4.6. Implications for arsenic mobility in anoxic environments

Although bacterial weathering of Fe(III)-bearing minerals can lead to release of associated elements to aqueous solutions, biogenic Fe(II)-containing reaction products are capable of scavenging a fraction of the soluble arsenic species. Our results reveal that biogenic FCH formed in the absence of arsenic is well-crystallized, whereas it is poorly crystalline in the presence of arsenic, suggesting that arsenic adsorbs on the particles during their nucleation/growth and passivates their surfaces. A similar influence of adsorbed arsenic on particle size has been previously observed by Waychunas et al. (1996) during the formation of ferrihydrite in the presence of arsenate, and by Wang et al. (2008) during the formation of magnetite in the presence of arsenite. Moreover, based on our Mössbauer results, we suggest that Fe(II) ions produced upon bacterial reduction of As(V)-adsorbed lepidocrocite co-precipitate with As(III) to form a minor As(III)–Fe(II)-containing solid phase identified as an $Fe(OH)_2$-like compound, which is mixed with dominant As(III)-adsorbed FCH. Under reducing conditions $97 \pm 3\%$ of As(III) is retained within solid phases during bioreduction of As(V)- and As(III)-adsorbed lepidocrocite, whereas only $54 \pm 2\%$ arsenic is sorbed on lepidocrocite after 10 days of incubation before inoculation with IRB cells (Fig. 2). These results indicate that, at least under some circumstances, bacterial reduction can promote As(III) sequestration in the form of As–Fe-containing biominerals.

ACKNOWLEDGMENTS

The authors are indebted to the SSRL staff, especially Joe Rogers, Samuel Webb, and William Butler, the ESRF-BM29 staff, especially Olivier Mathon, as well as the ELETTRA-XAFS & SOLEIL-SAMBA staff, especially Françoise Villain, for their technical assistance during the XAFS experiments. We acknowledge SSRL, ESRF, and ELETTRA for provision of beamtime through proposals 2781 & 3168, EC127, and 2006431, respectively. We thank AE Peggy O'Day and three anonymous reviewers for their constructive comments, which improved the quality of the manuscript. This work was supported by the ECCO-ECODYN and the EC2CO-CYTRIX CNRS/INSU Programs, by ACI/FNS Grant #3033, by SESAME IdF Grant #1775, by NSF-EMSI Grant CHE-0431425 (Stanford Environmental Molecular Science Institute), and by the France-Stanford Center for Interdisciplinary Studies. This is IPGP contribution # 2087.

APPENDIX A. Fe K-EXAFS DATA FOR THE BIOGENIC SAMPLES

Fe K-edge EXAFS data recorded at 10 K of the end-products of the bioreduction experiments, samples Lp-*Sp* #3, As(III)/Lp-*Sp* #7 and As(V)/Lp-*Sp* #9, are compared with EXAFS data of the R0.3 sample (As(III)-rich nano-$Fe(OH)_2$) in the following figure. Note the stronger second-neighbor contribution for this latter sample (R0.3), which is related to the presence of layers of FeO_6-octahedra in the $Fe(OH)_2$ structure, instead of double chains of FeO_6-octahedra in the FCH structure. (a) k^3-weighed $\chi(k)$ EXAFS, and (b) their corresponding Fourier transforms (FT), including the magnitude and imaginary part of the FT. Experimental and calculated curves are displayed as dashed and solid lines, respectively.

Corresponding shell-by-shell fitting parameters for samples Lp-*Sp* #3, As(III)/Lp-*Sp* #7 and As(V)/Lp-*Sp* #9 are reported in the following table, which shows their similarity with the malachite structure, taken as proxy for the FCH structure.

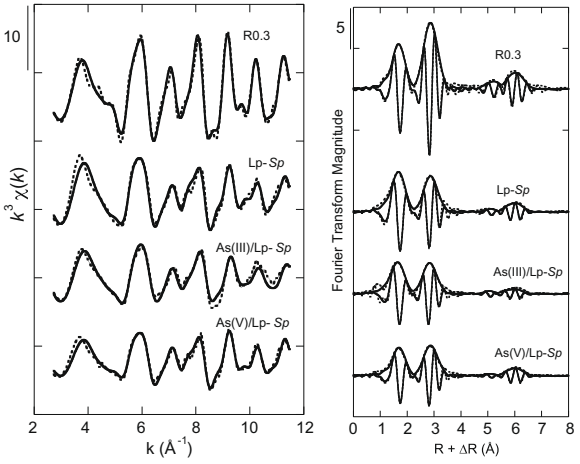

	Samples					Malachite structure[(A)]	
	R (Å)	N	σ (Å)	ΔE_0 (eV)	CHI^2_{FT}	<R (Å)>	N
Lp-*Sp* #3	2.12	3.9 Fe–O	0.09	4	0.06	2.15	6 Cu–O
	3.23	2.4 Fe–Fe	0.07	–		3.3	4 Cu–Cu
	5.6	1.0 Fe–Fe	–	–		5.4	10 Cu–Cu
	6.4	1.3 Fe–Fe–Fe–Fe	–	–		6.3	18 Cu–Cu
As(III)/Lp-*Sp* #7	2.09	3.2 Fe–O	0.09	5	0.06	6.5	6 Cu–Cu–Cu
	3.2	2.2 Fe–Fe	0.08	–		6.5	4 Cu–Cu–Cu–Cu
	5.5	0.8 Fe–Fe	–	–			
	6.4	0.8 Fe–Fe–Fe–Fe	–	–			
As(V)/Lp-*Sp* #9	2.13	2.2 Fe–O	0.08	6	0.04		
	3.22	1.6 Fe–Fe	0.07	–			
	5.6	1.6 Fe–Fe	–	–			
	6.4	0.9 Fe–Fe–Fe–Fe	–	–			

Note: R (Å): interatomic distances; N: number of neighbors; σ (Å): Debye Waller factor, ΔE_0 (eV): difference between the user-defined threshold energy and the experimentally determined threshold energy, in electron volts. During the fitting procedure, all parameter values indicated by (−) were linked to the parameter value placed above in the table. Errors on R and N values, estimated from the fit of the Fe K-edge EXAFS data for crystalline $Fe(OH)_2$ (Table 3), are ±0.02 and ±0.5 below $R = 4$ Å, ±0.05 and ±1.0 above $R = 4$ Å. Errors on σ and ΔE_0 values are ±0.01 and ±3, respectively. [(A)]Major single and multiple-scattering paths according to Feff8 analysis of the crystal structure of malachite $Cu_2(OH)_2CO_3$ (Zigan et al., 1977). Note that the structure of malachite is distorted due to Jahn–Teller effect characteristic of the electronic structure of the Cu^{2+} ion. Average interatomic path distances are reported here.

APPENDIX B. X-RAY POWDER DIFFRACTION DATA

X-ray powder diffraction (XRD) patterns of the $Fe(OH)_2$ sample, and those of the As(III)–Fe(II) (R0.1) and As(III)–Fe(II) (R0.3) model compounds samples are presented below. The glass capillaries used as sample containers yield a broad band at ~11.7° 2θ. The persistence of broad (1 0 0) and (1 1 0) Bragg reflections in the R0.1 and R0.3 patterns suggests that these compounds consist of nano-sized $Fe(OH)_2$ layers. The disappearing of the (00*l*) Bragg reflections indicates the quasi-absence of stacking along the *c* direction. According to the Scherrer formula, the average extension of the layers can be estimated as MCD[110] = 9.4 nm. These results are confirmed by EXAFS analysis (Fig. 6; Table 2).

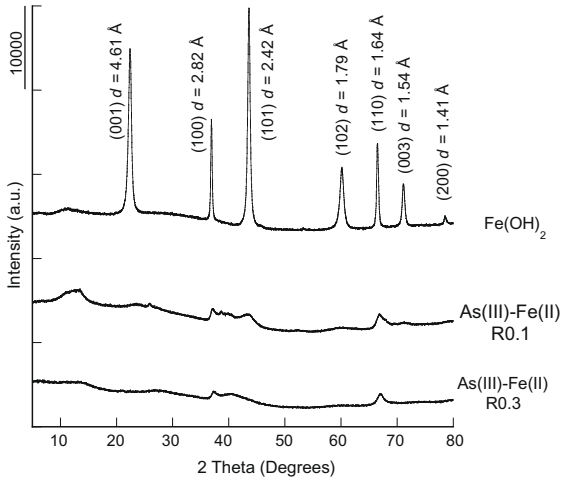

APPENDIX C. SUPPLEMENTARY DATA

Supplementary data associated with this article can be found, in the online version, at doi:10.1016/j.gca.2008.12.005.

REFERENCES

Ahmann D., Krumholz L. R., Hemond H. F., Lovley D. R. and Morel F. M. M. (1997) Microbial mobilization of arsenic from sediments of the Aberjona Watershed. *Environ. Sci. Technol.* **31**(10), 2923–2930.

Akai J., Izumi K., Fukuhara H., Masuda H., Nakano S., Yoshimura T., Ohfuji H., Md Anawar H. and Akai K. (2004) Mineralogical and geomicrobiological investigations on groundwater arsenic enrichment in Bangladesh. *Appl. Geochem.* **19**, 215–230.

Ankudinov A. L., Ravel B., Rehr J. J. and Conradson S. D. (1998) Real-space multiple-scattering calculation and interpretation of X-ray-absorption near-edge structure. *Phys. Rev. B* **58**, 7565–7576.

Armienta M. A., Villasenor G., Rodriguez R., Ongley L. K. and Mango H. (2001) The role of arsenic-bearing rocks in groundwater pollution at Zimapan Valley, Mexico. *Environ. Geol.* **40**, 571–581.

Ballirano P. and Maras A. (2002) Refinement of the structure of arsenolite, As_2O_3. *Zeits. Kristallogr.* **217**, 177–178.

Benali O., Abdelmoula M., Refait P. and Génin J.-M. R. (2001) Effect of orthophosphate on the oxidation products of Fe(II)–Fe(III) hydroxycarbonate: the transformation of green rust to ferrihydrite. *Geochim. Cosmochim. Acta* **65**(11), 1715–1726.

Bentley R. and Chasteen T. G. (2002) Microbial methylation of metalloids: arsenic, antimony, and bismuth. *Microbiol. Mol. Biol. Rev.* **66**(2), 250–271.

Bose P. and Sharma A. (2002) Role of iron in controlling speciation and mobilization of arsenic in subsurface environment. *Water Resour. Res.* **36**, 4916–4926.

Bourrié G., Trolard F., Génin J.-M. R., Jaffrezic A., Maitre V. and Abdelmoula M. (1999) Iron control by equilibria between

hydroxy-Green Rusts and solutions in hydromorphic soils. *Geochim. Cosmochim. Acta* **63**(19–20), 3417–3427.

Campbell K. M., Malasarn D., Saltikov C. W., Newman D. K. and Hering J. G. (2006) Simultaneous microbial reduction of iron(III) and arsenic(V) in suspensions of hydrous ferric oxide. *Environ. Sci. Technol.* **40**(19), 5950–5955.

Cancès B., Juillot F., Morin G., Laperche V., Alvarez L., Proux O., Hazemann J.-L., Brown, Jr., G. E. and Calas G. (2005) XAS evidence of As(V) association with iron oxyhydroxides in a contaminated soil at a former arsenical pesticide processing plant. *Environ. Sci. Technol.* **39**, 9398–9405.

Charlet L. and Polya D. A. (2006) Arsenic in shallow, reducing groundwaters in Southern Asia: an environmental health disaster. *Elements* **2**, 91–96.

Chichagov A. V., Belonozhko A. B., Lopatin A. L., Dokina T. N., Samokhvalova O. L., Ushakovskaya T. V. and Shilova Z. V. (1990) Information computing system from structural data on minerals (Mincryst). *Kristallografiya* **35**, 610–616.

Coker V. S., Gault A. G., Pearce C. I., van der Laan G., Telling N. D., Charnock J. M., Polya D. A. and Lloyd J. R. (2006) XAS and XMCD Evidence for species-dependent partitioning of arsenic during microbial reduction of ferrihydrite to magnetite. *Environ. Sci. Technol.* **40**, 7745–7750.

Cooper D. C., Picardal F., Rivera J. and Talbot C. (2000) Zinc immobilization and magnetite formation via ferric oxide reduction by *Shewanella putrefaciens* 200. *Environ. Sci. Technol.* **34**(1), 100–106.

Cooper M. A. and Hawthorne F. C. (1996) The crystal structure of ludlockite, $Pb(Fe^{3+})_4(As^{3+})_{10}O_{22}$, the mineral with pentameric arsenite groups and orange hair. *Canad. Mineral.* **34**, 79–89.

Cummings D. E., Caccavo F., Fendorf S. and Rosenzweig R. F. (1999) Arsenic mobilization by the dissimilatory Fe(III)-reducing bacterium *Shewanella alga* BrY. *Environ. Sci. Technol.* **33**(5), 723–729.

Dixit S. and Hering J. G. (2003) Comparison of arsenic(V) and arsenic(III) sorption onto iron oxide minerals: implications for arsenic mobility. *Environ. Sci. Technol.* **37**(18), 4182–4189.

Dowdle P. R., Laverman A. M. and Oremland R. S. (1996) Bacterial dissimilatory reduction of arsenic(V) to arsenic(III) in anoxic sediments. *Appl. Environ. Microbiol.* **62**(5), 1664–1669.

Drissi S. H., Refait P., Abdelmoula M. and Génin J.-M. R. (1995) The preparation and thermodynamic properties of iron(II)-iron(III) hydroxide-carbonate (green rust); Pourbaix diagram of iron in carbonate-containing aqueous media. *Corros. Sci.* **37**, 2025–2041.

Farquhar M. L., Charnock J. M., Livens F. R. and Vaughan D. J. (2002) Mechanisms of arsenic uptake from aqueous solution by interaction with goethite, lepidocrocite, mackinawite, and pyrite: an X-ray absorption spectroscopy study. *Environ. Sci. Technol.* **36**(8), 1757–1762.

Gault A. G., Islam F. S., Polya D. A., Charnock J. M., Boothman C., Chatterjee D. and Lloyd J. R. (2005) Microcosm depth profiles of arsenic release in a shallow aquifer, West Bengal. *Mineral. Mag.* **69**, 855–863.

Génin J.-M. R., Bourrié G., Trolard F., Abdelmoula M., Jaffrezic A., Refait P., Maître V., Humbert B. and Herbillon A. (1998) Thermodynamic equilibria in aqueous suspensions of synthetic and natural iron(II)-iron(III) green rusts: occurrences of the mineral in hydromorphic soils. *Environ. Sci. Technol.* **32**, 1058–1068.

Génin J.-M. R., Dhouibi L., Refait P., Abdelmoula M. and Triki E. (2002) Influence of phosphate on corrosion products of iron in chloride-polluted-concrete-simulating solutions: ferrihydrite vs green rust. *Corrosion* **58**(6), 467–478.

Génin J.-M. R., Olowe A. A., Refait P. and Simon L. (1996) On the stoichiometry and Pourbaix diagram of Fe(II)–Fe(III) hydroxy-sulphate or sulphate-containing green rust 2; an electrochemical and Mössbauer spectroscopy study. *Corros. Sci.* **38**, 1751–1762.

Glasauer S., Weidler P. G., Langley S. and Beveridge T. J. (2003) Controls on Fe reduction and mineral formation by a subsurface bacterium. *Geochim. Cosmochim. Acta* **67**(7), 1277–1288.

Graeser S., Schwander H., Demartin F., Gramaccioli C. M., Pilati T. and Reusser E. (1994) Fetiasite (Fe^{2+}, Fe^{3+}, $Ti)_3O_2$ $[As_2O_5]$, a new arsenite mineral—its description and structure determination. *Am. Mineral.* **79**, 996–1002.

Hansen H. C. B., Borggaard O. K. and Sorensen J. (1994) Evaluation of the free energy of formation of Fe(II)–Fe(III) hydroxide-sulphate (green rust) and its reduction of nitrite. *Geochim. Cosmochim. Acta* **58**(12), 2599–2608.

Harvey C. F., Swartz C. H., Badruzzaman A. B. M., Keon-Blute N., Yu W., Ali M. A., Jay J., Beckie R., Niedan V. and Brabander D. (2005) Groundwater arsenic contamination on the Ganges Delta: biogeochemistry, hydrology, human perturbations, and human suffering on a large scale. *Comptes Rendus Geosciences* **337**, 285–296.

Harvey C. F., Swartz C. H., Badruzzaman A. B. M., Keon-Blute N., Yu W., Ali M. A., Jay J., Beckie R., Niedan V., Brabander D., Oates P. M., Ashfaque K. N., Islam S., Hemond H. F. and Ahmed M. F. (2002) Arsenic mobility and groundwater extraction in Bangladesh. *Science* **298**, 1602–1606.

Hawthorne F. C. (1985) Schneiderhöhnite, $Fe^{2+}(Fe^{3+})_3(As^{3+})_5O_{13}$, a densely packed arsenite structure. *Canad. Mineral.* **23**, 675–679.

Horneman A., Van Geen A., Kent D. V., Mathe P. E., Zheng Y., Dhar R. K., O'Connell S., Hoque M. A., Aziz Z., Shamsudduha M., Seddique A. A. and Ahmed K. M. (2004) Decoupling of As and Fe release to Bangladesh groundwater under reducing conditions. Part 1: evidence from sediment profiles. *Geochim. Cosmochim. Acta* **68**, 3459–3473.

Islam F. S., Gault A. G., Boothman C., Polya D. A., Charnock J. M., Chatterjee D. and Lloyd J. R. (2004) Role of metal-reducing bacteria in arsenic release from Bengal delta sediments. *Nature* **430**, 68–71.

Joanne M. S., Lindsay I. S., Aimin W., Dean C., Pascal De W.-D. and Joan M. M. (2002) New arsenite-oxidizing bacteria isolated from australian gold mining environments—phylogenetic relationships. *Geomicrobiol. J.* **19**(1), 67–76.

Klingelhofer G., Morris R. V., Bernhardt B., Schroder C., Rodionov D. S., de Souza P. A., Yen A., Gellert R., Evlanov E. N., Zubkov B., Foh J., Bonnes U., Kankeleit E., Gutlich P., Ming D. W., Renz F., Wdowiak T., Squyres S. W. and Arvidson R. E. (2004) Jarosite and hematite at Meridiani Planum from Opportunity's Mossbauer spectrometer. *Science* **306**(5702), 1740–1745.

Kocar B. D., Herbel M. J., Tufano K. J. and Fendorf S. (2006) Contrasting effects of dissimilatory iron(III) and arsenic(V) reduction on arsenic retention and transport. *Environ. Sci. Technol.* **40**(21), 6715–6721.

Kukkadapu R. K., Zachara J. M., Fredrickson J. K. and Kennedy D. W. (2004) Biotransformation of two-line silica-ferrihydrite by a dissimilatory Fe(III)-reducing bacterium: formation of carbonate green rust in the presence of phosphate1. *Geochim. Cosmochim. Acta* **68**(13), 2799–2814.

Kukkadapu R. K., Zachara J. M., Fredrickson J. K., Kennedy D. W., Dohnalkova A. C. and McCready D. E. (2005) Ferrous hydroxy carbonate is a stable transformation product of biogenic magnetite. *Am. Mineral.* **90**(2–3), 510–515.

Lagarec K. and Rancourt D. G. (1997) Extended Voigt-based analytic lineshape method for determining N-dimensional correlated hyperfine parameter distributions in Mossbauer spectroscopy. *Nucl. Instrum. Methods Phys. Res. Sect. B-Beam Interact. Mater. Atoms* **129**(2), 266–280.

Legrand L., Sagon G., Lecomte S., Chausse A. and Messina R. (2001) A Raman and infrared study of a new carbonate green rust obtained by electrochemical way. *Corros. Sci.* **43**(9), 1739–1749.

Lovley D. R., Stolz J. F., Nord G. L. and Phillips E. J. P. (1987) Anaerobic production of magnetite by a dissimilatory iron-reducing microrganism. *Nature* **330**, 252–254.

Manning B. A., Fendorf S. E. and Goldberg S. (1998) Surface structures and stability of arsenic(III) on goethite: spectroscopic evidence for inner-sphere complexes. *Environ. Sci. Technol.* **32**(16), 2383–2388.

Manning B. A., Hunt M. L., Amrhein C. and Yarmoff J. A. (2002) Arsenic(III) and arsenic(V) reactions with zerovalent iron corrosion products. *Environ. Sci. Technol.* **36**(24), 5455–5461.

McArthur J. M., Ravenscroft P., Safiulla S. and Thirlwall M. F. (2001) Arsenic in groundwater: Testing pollution mechanisms for sedimentary aquifers in Bangladesh. *Water Resources Res.* **37**, 109–117.

Morin G. and Calas G. (2006) Arsenic in soils, mine tailings, and former industrial sites. *Elements* **2**(2), 97–101.

Morin G., Juillot F., Casiot C., Bruneel O., Personne J. C., Elbaz-Poulichet F., Leblanc M., Ildefonse P. and Calas G. (2003) Bacterial formation of tooeleite and mixed arsenic(III) or arsenic(V)-iron(III) gels in the Carnoules acid mine drainage, France. A XANES, XRD, and SEM study. *Environ. Sci. Technol.* **37**, 1705–1712.

Morin G., Ona-Nguema G., Wang Y., Menguy N., Juillot F., Proux O., Guyot F., Calas G. and Brown, Jr., G. E. (2008) EXAFS analysis of arsenite and arsenate adsorption on maghemite. *Environ. Sci. Technol. Environ. Sci. Technol.* **42**, 2361–2366.

Morin G., Rousse G. and Elkaim E. (2007) Crystal structure of tooeleite, $Fe_6(AsO_3)_4SO_4(OH)_4{\cdot}4H_2O$, a new iron arsenite oxyhydroxysulfate mineral relevant to acid mine drainage. *Am. Mineral.* **92**, 193–197.

Newman D. K., Ahmann D. and Morel F. M. M. (1998) A brief review of microbial arsenate respiration. *Geomicrobiol. J.* **15**(4), 255–268.

Nickson R. T., McArthur J., Burgess W., Ahmed K. M., Ravenscroft P. and Rahmann M. (1998) Arsenic poisoning of Bangladesh groundwater. *Nature* **395**, 338.

Nickson R. T., McArthur J. M., Ravenscroft P., Burgess W. G. and Ahmed K. M. (2000) Mechanism of arsenic release to groundwater, Bangladesh and West Bengal. *Appl. Geochem.* **15**, 403–413.

Nriagu J. (2002) Arsenic poisoning through the ages. In *Environmental Chemistry of Arsenic pp. 21–22* (ed. W. T. Frankenberger). M. Dekker.

O'Loughlin E. J., Larese-Casanova P., Scherer M. and Cook R. (2007) Green rust formation from the bioreduction of gamma-FeOOH (lepidocrocite): Comparison of several *Shewanella* species. *Geomicrobiol. J.* **24**(3–4), 211–230.

Ona-Nguema G., Abdelmoula M., Jorand F., Benali O., Géhin A., Block J.-C. and Génin J.-M. R. (2002a) Iron(II, III) hydroxycarbonate green rust formation and stabilization from lepidocrocite bioreduction. *Environ. Sci. Technol.* **36**(1), 16–20.

Ona-Nguema G., Abdelmoula M., Jorand F., Benali O., Géhin A., Block J.-C. and Génin J.-M. R. (2002b) Microbial reduction of lepidocrocite γ-FeOOH by *Shewanella putrefaciens*; the formation of a green rust. *Hyperfine Interact.* **139**(140), 231–237.

Ona-Nguema G., Carteret C., Benali O., Abdelmoula M., Génin J.-M. R. and Jorand F. (2004) Competitive formation of hydroxycarbonate green rust I vs hydroxysulphate green rust II in *Shewanella putrefaciens* cultures. *Geomicrobiol. J.* **21**(3), 79–90.

Ona-Nguema G., Jorand F., Benali O., Abdelmoula M., Génin J.-M. R., and Block J.-C. (2001) Key role of the kinetics of g-FeOOH bioreduction on the formation of Fe(II)-Fe(III) minerals. In: W. J. Thomas MF, Gibb TC (Eds.), *Proceedings of the International Conference on the Applications of the Mössbauer Effect (ICAME 2001). Hyperfine Interactions (C)*, Vol. 5 , pp. 415–418. Dordrecht: Kluwer Academic Publishers.

Ona-Nguema G., Morin G., Juillot F., Calas G. and Brown, Jr., G. E. (2005) EXAFS analysis of arsenite adsorption onto two-line ferrihydrite, hematite, goethite, and lepidocrocite. *Environ. Sci. Technol.* **39**(23), 9147–9155.

Oremland R. S. and Stolz J. F. (2003) The ecology of arsenic. *Science* **300**, 939–944.

Parmar N., Gorby Y. A., Beveridge T. J. and Ferris F. G. (2001) Formation of green rust and immobilization of nickel in response to bacterial reduction of hydrous ferric oxide. *Geomicrobiol. J.* **18**(4), 375–385.

Polizzotto M.L., D. Kocar B.D., Benner S.G., Sampson M. and Fendorf S. (2008) Near-surface wetland sediments as a source of arsenic release to ground water in Asia. *Nature* **454**, 505–508.

Polizzotto M. L., Harvey C. F., Sutton S. R. and Fendorf S. (2005) Processes conducive to the release and transport of arsenic into aquifers of Bangladesh. *Proc. Natl. Acad. Sci. USA* **102**(52), 18819–18823.

Randall S. R., Sherman D. M. and Ragnarsdottir K. V. (2001) Sorption of As(V) on green rust ($Fe^{II}_4Fe^{III}_2(OH)_{12}SO_4$ center dot $3H_2O$) and lepidocrocite (gamma-FeOOH): surface complexes from EXAFS spectroscopy. *Geochim. Cosmochim. Acta* **65**(7), 1015–1023.

Refait P. and Génin J.-M. R. (1993) The oxidation of ferrous hydroxide in chloride-containing aqueous media and Pourbaix diagrams of green rust one. *Corros. Sci.* **34**, 797–819.

Refait P., Abdelmoula M. and Génin J.-M. R. (1998a) Mechanisms of formation and structure of green rust one in aqueous corrosion of iron in the presence of chloride ions. *Corros. Sci.* **40**(9), 1547–1560.

Refait P., Abdelmoula M., Génin J.-M. R. and Jeannin M. (2006) Synthesis and characterization of the Fe(II–III) hydroxyformate green rust. *Hyperfine Interact.* **167**(1–3), 717–722.

Refait P., Abdelmoula M., Trolard F., Génin J.-M. R., Ehrhardt J. J. and Bourrié G. (2001) Mössbauer and XAS study of a green rust mineral; the partial substitution of Fe^{2+} by Mg^{2+}. *Am. Mineral.* **86**(5–6), 731–739.

Refait P., Charton A. and Génin J.-M. R. (1998b) Identification, composition, thermodynamic and structural properties of a pyroaurite-like iron(II)–iron(III) hydroxyoxalate Green Rust. *Eur. J. Solid State Inorg. Chem.* **35**(10–11), 655–666.

Refait P., Gehin A., Abdelmoula M. and Genin J.-M. R. (2003) Coprecipitation thermodynamics of iron (II-III) hydroxysulphate green rust from Fe (II) and Fe (III) salts. *Corros. Sci.* **45**(4), 659–676.

Root R. A., Dixit S., Kate M., Campbell K. M., Jew A. D., Janet G., Hering J. G. and O'Day P. A. (2007) Arsenic sequestration by sorption processes in high-iron sediments. *Geochim. Cosmochim. Acta* **71**, 5782–5803.

Simon L., Francois M., Refait P., Renaudin G., Lelaurain M. and Génin J.-M. R. (2003) Structure of the Fe(II–III) layered double hydroxysulphate green rust two from Rietveld analysis. *Solid State Sci.* **5**, 327–334.

Simon L., Génin J.-M. R. and Refait P. (1997) Standard free enthalpy of formation of Fe(II)–Fe(III) hydroxysulphite green rust one and its oxidation into hydroxysulphate green rust two. *Corros. Sci.* **39**(9), 1673–1685.

Smedley P. L. and Kinniburgh D. G. (2002) A review of the source, behaviour and distribution of arsenic in natural waters. *Appl. Geochem.* **17**, 517–568.

Stolz J. F. and Oremland R. S. (1999) Bacterial respiration of arsenic and selenium. *FEMS Microbiol. Rev.* **23**(5), 615–627.

Thoral S., Rose J., Garnier J. M., Van Geen A., Refait P., Traverse A., Fonda E., Nahon D. and Bottero J. Y. (2005) XAS study of

iron and arsenic speciation during Fe(II) oxidation in the presence of As(III). *Environ. Sci. Technol.* **39**, 9478–9485.

Trolard F., Bourrie G., Abdelmoula M., Refait P. and Feder F. (2007) Fougerite, a new mineral of the pyroaurite-iowaite group: description and crystal structure. *Clays Clay Minerals* **55**(3), 323–334.

Trolard F., Génin J.-M. R., Abdelmoula M., Bourrié G., Humbert B. and Herbillon A. (1997) Identification of a green rust mineral in a reductomorphic soil by Mössbauer and Raman spectroscopy. *Geochim. Cosmochim. Acta* **61**, 1107–1111.

van Geen A., Rose J., Thoral S., Garnier J. M., Zheng Y. and Bottero J. Y. (2004) Decoupling of As and Fe release to Bangladesh groundwater under reducing conditions. Part II: evidence from sediment incubations. *Geochim. Cosmochim. Acta* **68**(17), 3475–3486.

Vaughan D. J. (2006) Arsenic. *Elements* **2**(2), 71–75.

Venkateswaran K., Moser D. P., Dollhopf M. E., Lies D. P., Saffarini D. A., MacGregor B. J., Ringelberg D. B., White D. C., Nishijima M., Sano H., Burghardt J., Stackebrandt E. and Nealson K. H. (1999) Polyphasic taxonomy of the genus *Shewanella* and description of *Shewanella oneidensis* sp. Nov.. *Int. J. Syst. Bacteriol.* **49**(Pt. 2), 705–724.

Wang Y., Morin G., Ona-Nguema G., Menguy N., Juillot F., Aubry E., Guyot F., Calas G. and Brown, Jr., G. E. (2008) Arsenite sorption at the magnetite–water interface during aqueous precipitation of magnetite at neutral pH. *Geochim. Cosmochim. Acta* **72**, 2573–2586.

Waychunas G. A., Fuller C. C., Rea B. A. and Davis J. A. (1996) Wide angle X-ray scattering (WAXS) study of "two-line" ferrihydrite structure: effect of arsenate sorption and counterion variation and comparison with EXAFS results. *Geochim. Cosmochim. Acta* **60**(10), 1765–1781.

Waychunas G. A., Xu N., Fuller C. C., Davis J. A. and Bigham J. M. (1995) XAS study of AsO_4^{3-} and SeO_4^{2-} substituted schwertmannites. *Physica B* **208–209**(1–4), 481–483.

Wilke M., Farges F., Petit P. E., Brown, Jr., G. E. and Martin F. (2001) Oxidation state and coordination of Fe in minerals: an FeK-XANES spectroscopic study. *Am. Mineral.* **86**, 714–730.

Wilkie J. A. and Hering J. G. (1998) Rapid oxidation of geothermal arsenic(III) in streamwaters of the Eastern Sierra Nevada. *Environ. Sci. Technol.* **32**(5), 657–662.

Winterer M. (1997) XAFS—a data analysis program for materials science. *J. de Physique IV* **7**, 243–244.

Xu H., Zhao Y., Vogel S. C., Daemen L. L. and Hickmott D. D. (2007) Anisotropic thermal expansion and hydrogen bonding behavior of portlandite: a high-temperature neutron diffraction study. *J. Solid State Chem.* **180**, 1519–1525.

Zachara J. M., Kukkadapu R. K., Fredrickson J. K., Gorby Y. A. and Smith S. C. (2002) Biomineralization of poorly crystalline Fe(III) oxides by dissimilatory metal reducing bacteria (DMRB). *Geomicrobiol. J.* **19**(2), 179–207.

Zegeye A., Huguet L., Abdelmoula M., Carteret C., Mullet M. and Jorand F. (2007) Biogenic hydroxysulfate green rust, a potential electron acceptor for SRB activity. *Geochim. Cosmochim. Acta* **71**(22), 5450–5462.

Zegeye A., Ona-Nguema G., Carteret C., Huguet L., Abdelmoula M. and Jorand F. (2005) Formation of hydroxysulphate green rust 2 as a single iron(II–III) mineral in microbial culture. *Geomicrobiol. J.* **22**, 1–11.

Zigan F. and Rothbauer R. (1967) Neutronenbeugungsmessungen am Brucit. *Neues Jb. Miner., Mh.*, 137–143.

Zigan F., Joswig W. and Schuster H. D. (1977) Refinement of the structure of malachite, $Cu_2(OH)_2CO_3$, by means of neutron-diffraction. *Zeits. Kristallogr.* **145**, 412–426.

Zobrist J., Dowdle P. R., Davis J. A. and Oremland R. S. (2000) Mobilization of arsenite by dissimilatory reduction of adsorbed arsenate. *Environ. Sci. Technol.* **34**(22), 4747–4753.

Associate editor: Peggy A. O'Day